



HAL
open science

Storage conditions and eruptive dynamics of central versus flank eruptions in volcanic islands: the case of Tenerife (Canary Islands, Spain)

Joan Andújar, Fidel Costa, Bruno Scaillet

► To cite this version:

Joan Andújar, Fidel Costa, Bruno Scaillet. Storage conditions and eruptive dynamics of central versus flank eruptions in volcanic islands: the case of Tenerife (Canary Islands, Spain). *Journal of Volcanology and Geothermal Research*, 2013, 260, pp.62-79. 10.1016/j.jvolgeores.2013.05.004 . insu-00827722

HAL Id: insu-00827722

<https://insu.hal.science/insu-00827722>

Submitted on 29 May 2013

HAL is a multi-disciplinary open access archive for the deposit and dissemination of scientific research documents, whether they are published or not. The documents may come from teaching and research institutions in France or abroad, or from public or private research centers.

L'archive ouverte pluridisciplinaire **HAL**, est destinée au dépôt et à la diffusion de documents scientifiques de niveau recherche, publiés ou non, émanant des établissements d'enseignement et de recherche français ou étrangers, des laboratoires publics ou privés.

Storage conditions and eruptive dynamics of central versus flank eruptions in volcanic islands: the case of Tenerife (Canary Islands, Spain)

Joan Andújar^{a,*}, Fidel Costa^b, Bruno Scaillet^a

a. Université d'Orléans, ISTO, UMR 7327, 45071, Orléans, France ; CNRS/INSU, ISTO, UMR 7327, 45071 Orléans, France ; BRGM, ISTO, UMR 7327, BP 36009, 45060 Orléans, France.

b. Earth Observatory of Singapore, Nanyang Technological University, Singapore 639798, Singapore

* **Corresponding author:** Joan Andújar.

phone number: (+33) 2 38 25 53 87

Fax: (+33) 02 38 63 64 88

e-mail address: Juan.Andujar@cnrs-orleans.fr

Fidel Costa e-mail address: fcosta@ntu.edu.sg

Bruno Scaillet e-mail address: bscaille@cnrs-orleans.fr

KEY WORDS: *Phase equilibria, phonolite, experimental petrology, eruptive dynamic, flank eruption, central eruption, Tenerife, Teide.*

Abstract

We report the results of phase equilibrium experiments on a phonolite produced during one of the most voluminous flank eruptions (ca. 1 km³) of the Teide-Pico Viejo complex (Tenerife Island). Combined with previous experimental and volcanological data we address the factors that control the structure of the phonolitic plumbing system of Teide-Pico Viejo stratovolcanoes. The Roques Blancos phonolite erupted ca 1800 BP and contains ~14 wt % phenocrysts, mainly anorthoclase, biotite, magnetite, diopside and lesser amounts of ilmenite. Crystallization experiments were performed at temperatures of 900°C, 850°C and 800°C, in the pressure range 200 MPa to 50 MPa. The oxygen fugacity (f_{O_2}) was varied between NNO+0.3 (0.3 log units above to the Ni-NiO solid buffer) to NNO-2, whilst dissolved water contents varied from 7 wt% to 1.5 wt%. The comparison between natural and experimental phase proportions and compositions, including glass, indicates that the phonolite magma was stored prior to eruption at 900±15°C, 50±15MPa, with about 2.2 wt% H₂O dissolved in the melt, at an oxygen fugacity of NNO-0.5 (±0.5). The difference in composition between the rim and the cores of the natural anorthoclase phenocrysts suggests that the phonolite was heated by about 50°C before the eruption, upon intrusion of a hotter tephriphonolitic magma. The comparison between the storage conditions of Roques Blancos and those inferred for other phonolites of the Teide-Pico Viejo volcanic complex shows that flank eruptions are fed by reservoirs located at relatively shallow depths (1-2 km) compared to those feeding Teide central eruptions (5 km).

1. Introduction

Understanding the plumbing system beneath volcanic edifices is crucial to constrain the parameters that control the evolution of ascending magmas and for anticipating the future eruptive behaviour of the volcano. The use of dense geophysical and geochemical monitoring networks deployed on highly active volcanoes (i.e., Etna volcano; Bonaccorso et al. 2004) allows to gain information concerning the movement and likely levels of magma storage. Monitoring data combined with petrological studies (e.g., Kahl et al., 2011) enables to better reconstruct the geometry of the plumbing system beneath the volcanic edifice of an on-going eruption, and thus construct more robust eruptive scenarios in the short time frame.

However, real time monitoring techniques do not easily allow to understand the mid (e.g., hundred years) to long-term (thousands of year or more) evolution of the volcanic system, or the variation of eruptive dynamics (ie.; variation in eruptive style during a single event or between eruptions) with time. This is particularly true for volcanoes with low eruption frequency, which are characterised by long periods of dormancy during which little, if any, geophysical or geochemical signals can be recorded, making their interpretations difficult whenever the system awakes. The volcanological record often bears witness of significant variations in the eruptive styles (alternation between sustained explosive Plinian eruptions, transient explosive and purely effusive activity), and in vent location (central and flank eruptions; i.e., Corsaro et al., 2007; Ablay and Martí, 2000), which may in part reflect the complexity of the plumbing system. In such cases, only the study of past eruptions and the distribution of eruptive centres can provide insights on both the long-term evolution of the volcanic edifices and on the factors that control the eruptive dynamic.

This is the case of Tenerife in the Canary Islands, a volcanic island that has slowly evolved from a primitive to highly differentiated edifice. The spatial and temporal distribution of its recent volcanism demonstrates that the island is highly active (Martí et al., 2008), yet eruptions are spaced in time, events being separated by x100-1000 years (Carracedo et al., 2007; Martí et al., 2008). Tenerife island hosts the active Teide-Pico Viejo volcano, which is characterised by emission of magmas from either central (Teide main vent) or flank vents. Despite a diversity of eruptive styles during the last 35 kyrs, erupted magmas have similar phonolitic compositions (Ablay et al., 1995; Ablay et al., 1998; Rodríguez-Badiola et al, 2006; Carracedo and Rodríguez-

Badiola, 2006; Carracedo et al., 2007; Martí et al., 2008; Wiesmaier et al., 2012). Recent numerical simulations performed on this volcanic complex suggest that the main factors controlling the vent location at Teide-Pico Viejo are the shape of the reservoir and the stress field distribution around it which can be affected by the presence of a second magma chamber (Martí and Geyer, 2009). Such a possibility is supported by the petrological and geochronological data of recent phonolitic eruptions (Ablay et al., 1998; Carracedo et al., 2007; Andújar and Scaillet, 2012a). The relative position between the reservoirs also exerts an important control on the final trajectory of the injected dykes and hence in the final location (central or flank) of the vent (Martí and Geyer, 2009). Since the depths of such reservoirs feeding flank eruptions at Teide-Pico Viejo are poorly constrained (Andújar and Scaillet, 2012a), we have performed phase equilibrium experiments on a representative phonolite of the Roques Blancos, one of the most recent flank dome eruptions occurred at this volcanic island.

2. Geological setting

The evolution and stratigraphy of Teide stratovolcano have been the focus of several studies (i.e., Araña, 1971; Martí et al., 1994; Ablay et al., 1998; Martí and Gudmunsson, 2000; Ablay and Martí, 2000; Rodríguez-Badiola et al., 2006; Carracedo et al., 2007; Wiesmaier et al., 2012). We first summarise the main aspects concerning the structural and volcanological evolution of the actual volcanic complex of Teide and Pico Viejo stratovolcanoes.

The post-shield volcanism of Tenerife has been characterised by the repetitive development of compositionally evolved centres including 3 caldera collapses (Martí et al., 1994; Ablay et al., 1998; Carracedo et al., 2007). The products of the last and most recent eruptive cycle (< 200 kyr) built the twin stratovolcano of Teide and Pico Viejo (T-PV). The most recent volcanism includes that of the main T-PV cones which is characterised by the emission of significant volumes of phonolitic magmas, and the volumetrically smaller and more mafic eruptions from the rifts (Martí et al., 1994; Ablay and Martí, 2000; Carracedo et al., 2007; Martí et al., 2008). The extrusion of mafic to intermediate magmas dominated the first stages of the construction of the T-PV volcanic complex until 35 ka ago. Then, phonolitic magmas started to erupt and became the predominant erupted composition till today (Ablay et al., 1998; Rodríguez-Badiola et al., 2006; Carracedo et al., 2007). During the last 35 ka, magma emission occurred

either at central Pico Teide or from the numerous flank vents (up to 10), of which the Montaña Blanca, Roques Blancos, Pico Cabras and Montaña Rajada events are the most important ones (Fig.1b; Ablay and Martí, 2000; Rodríguez-Badiola et al., 2006; Carracedo et al., 2007).

Although such satellite eruptions are volumetrically smaller (generally $\leq 0.2 \text{ km}^3$) relative to those from the central Teide vent (generally $\geq 0.3 \text{ km}^3$), they are characterised by a sustained explosive activity and fall-out deposits together with the emission of thick lava flows (García et al., 2012; Martí et al., 2012). The explosive activity of these flank eruptions includes the sub-Plinian event of Montaña Blanca (Ablay et al., 1995; Ablay and Martí, 2000; Rodríguez-Badiola et al., 2006; Martí et al., 2008; Andújar and Scaillet, 2012a), and El Boqueron flank eruption (García et al., 2012). In addition to these episodes, two more phonolitic explosive flank events have been recently identified (Martí et al., 2012; O. García unpublished data). In contrast, phonolitic volcanism from Teide proper is less explosive, and alternates between pure effusive activity that generated thick lava flows and transient explosive activity, which has produced scoria and spatter deposits (Ablay and Martí, 2000; Martí et al., 2008). However, it is unclear why some eruptions proceed through the central Teide cone while others occur on its flanks, and how does this relate to the more explosive activity from the flank events. Here we provide petrological constraints to explain these observations by determining the pre-eruptive conditions of the Roques Blancos dome, one of the most significant flank eruptions in the recent history of Teide-Pico Viejo volcanic complex, in terms of the erupted volume and extension of the lava flows (Fig.1; Balcells and Hernández-Pacheco, 1989; Carracedo and Rodríguez-Badiola, 2006; Martí et al., 2008).

3. The Roques Blancos eruption

The Roques Blancos event occurred in two eruptive episodes, the oldest one (1974 BP) from a satellite dome located at the NW side of Pico Viejo stratovolcano at about 2800 m asl (above sea level) and, a second eruption occurring at 1714 BP from a dome located a few hundred meters below the first vent (2500-2600 m asl; Fig. 1; Balcells and Hernández-Pacheco, 1989; Carracedo and Rodríguez-Badiola, 2006; Carracedo et al., 2007). These eruptions emitted about 0.8 to 1 km^3 of highly evolved phonolitic magma which covered a surface of about 15 km^2 and generated lava that flowed over a height difference of about 3000 m, reaching the seaside in the Northern

part of Tenerife Island (Carracedo and Rodríguez-Badiola 2006; Martí et al., 2012). Both phonolitic products are petrologically and geochemically very similar (Fig.1; Balcells and Hernández-Pacheco, 1989; Ablay, 1997; Ablay et al., 1998; Ablay and Martí, 2000; Carracedo and Rodríguez-Badiola, 2006; Carracedo et al., 2007; Martí et al., 2008).

3.1. Pre-eruptive conditions of Roques Blancos magma from petrological observations

Several blocks of lava were collected at ~ 2500 m asl from one of the main lava flows of the 1714 BP Roques Blancos youngest dome (Fig.1). The freshest rock blocks were selected as starting material for performing phase equilibrium experiments, whole-rock, and electron microprobe analyses (EMPA) of the different phases (Table 1). The bulk-rock composition, as determined by ICP-MS, is a typical phonolite (59.4 wt% SiO₂, 15.4 Na₂O+K₂O; Le Maitre et al., 1989; Table 1) representative of the Roques Blancos flows (Balcells and Hernández-Pacheco, 1989; Ablay et al., 1998; Carracedo and Rodríguez-Badiola, 2006).

Modal point counting of three thin sections (3000 points each) was combined with mineral densities to obtain the weight percent (wt%) of the different phases. The sample has ~14 wt % phenocrysts, mainly anorthoclase (13.7 wt%; An₄₋₃, Ab₆₉₋₆₅, Or₃₂₋₂₇), minor amounts of biotite (0.3 wt%; Mg#62-63; Mg#=100[Mg/(Mg+Fe*)]), magnetite (0.3 wt%; Mg# 5), diopside (0.1 wt%; Mg# 68-70; En₃₉₋₄₁,Fs₉₋₁₁,Wo₅₀) and ilmenite (0.1 wt%). Phenocrysts are set in a highly crystalline groundmass made of microlites of alkali feldspar, magnetite, clinopyroxene, in addition to glass (Table 1, Fig.2). Mass-balance calculations were used to obtain the composition of the residual melt that was in equilibrium with phenocrysts by combining the whole-rock and mineral phase compositions. As anticipated owing to the low phenocryst content, the resulting melt is phonolitic (59.2 wt% SiO₂, 17.0 wt% Na₂O+K₂O) with a composition similar to that of the bulk-rock (Table 1).

Backscattered electron images (BSE) of the sample show that most anorthoclase phenocrysts show prominent bright rims and dissolution surfaces, while clinopyroxene displays oscillatory zoning and some dissolution surfaces, and some Fe-Ti oxides present exsolution textures whereas others do not. In contrast, biotite appears to be homogeneous on BSE. Elemental mapping of Ba and EMPA traverses of anorthoclase reveal core to rim zonations (cores at An_{2.5-4} and BaO 0.1-0.2 wt%, toward more

calcium- and Ba-rich rims of An₇₋₈ and up to 0.4 wt%, respectively; Fig.3). In detail, many crystals show complex rims: (1) the outermost rims (e.g., last 10-20 μm) have extremely high Fe and Ti, high Ca, and very low Ba, possibly resulting from fast growth, during which incompatible elements are incorporated at higher than equilibrium concentrations, and compatible ones at lower than equilibrium concentrations (e.g., Albarède and Bottinga, 1972). (2) Inside this outer rim, crystals still have a high Fe, Ti, Ca and Ba zones, compared to the core. There is a dissolution zone between the inner part and the outer rims of the crystals. These observations suggest that there was a change in the pre-eruptive conditions just prior to eruption, i.e. magma reheating upon a recharge event, followed by a fast crystal growth stage.

Pre-eruptive temperatures and $f\text{O}_2$ for the 1714 BP Roques Blancos phonolite were determined by using six co-existing Fe-Ti oxides and the thermo-oxybarometric model of Sauerzapf et al. (2008). Results yield temperatures of $895\pm 5^\circ\text{C}$ and a $\log f\text{O}_2$ of -12.2, equivalent to an oxygen fugacity of 0.2 log units below the Ni-NiO solid buffer (NNO-0.2; Table 1). As there are currently no constraints on storage pressure or volatile content of the Roques Blancos phonolite, the ranges of pressure and volatile content covered in the experiments were guided by previous results obtained on similar compositions of the same volcanic complex (Andújar et al., 2010; Andújar and Scaillet, 2012a).

4. Experimental work

We have performed phase-equilibrium experiments following a methodology similar to that used for constraining the storage conditions of active volcanoes such as Stromboli, Vesuvius, St. Pedro volcanoes (e.g., Di Carlo et al., 2006; Scaillet et al., 2008; Costa et al., 2004) and taking in account the recommendations in the application of phase equilibrium experiments to volcanic rocks as laid down by Pichavant et al. (2007).

4.1. Preparation of the starting material

Pieces of the phonolitic lava were finely ground in an agate mortar and then melted in a Pt crucible at 1400°C during 5 hours in open-air atmosphere. The sample was quenched in a water container at room temperature, glass chips recovered ground again and re-melted. Chips of the resulting starting glass were analysed by the EMP and compared to the bulk-rock composition, showing that it is homogeneous with no

significant Na or Fe loss compared to the starting rock (Table 1). The dry glass was then ground for obtaining a powder that was used as starting material for hydrothermal experiments and stored in an oven at 120°C.

4.2. Experimental equipment and procedures

A total of 55 crystallization experiments were performed at the experimental laboratory of ISTO (Orléans, France) in a vertically operating Internally Heated Pressure Vessel (IHPV), using Ar as pressurising medium which was mixed with different amounts of H₂ at room temperature in order to achieve different fO_2 (Scaillet et al., 1992). A transducer calibrated against a Heise Bourdon gauge with an uncertainty of ± 2 MPa was used for recording total pressure. Experiments were performed using double-winding molybdenum and kanthal furnaces which produce near-isothermal conditions (gradient $< 2\text{-}3^\circ\text{C}/\text{cm}$) along a 3 cm long hot spot. S- or K-type thermocouples with an accuracy of $\pm 5^\circ\text{C}$ were used to record experimental temperature and a rapid-quench technique was systematically used which allows isobaric quenches at high cooling rates ($> 100^\circ\text{C}/\text{s}$) (e.g., Martel et al., 1999; Di Carlo et al., 2006). In all runs reported here, the drop quench was successful as indicated by the rise in total pressure upon the falling of the sample holder into the cold (bottom) part of the vessel.

Experiments were mainly conducted at 850 °C and 900 °C, pressures of 200, 150, 100, and 50 MPa and at $fO_2 \sim \text{NNO}+0.3$ to $\text{NNO}-2$. The effect of temperature on phase relationships and compositions was studied by conducting experiments at 800°C, 200 and 100 MPa at $\sim \text{NNO}$. One run was also performed at $\text{NNO}-1$ at 850 °C and 100 MPa so as to study the effect of oxygen fugacity on phase equilibria at this temperature (Table 2).

4.2.1. Capsule preparation

H₂O-saturated and undersaturated charges were prepared using 1.5 cm long, 2.5 mm inner diameter, 0.2 mm wall thickness Au capsules. Distilled H₂O was first loaded, then silver oxalate as the source of CO₂ for H₂O-undersaturated charges, and finally the glass powder was introduced. Capsules were weighed and then welded using a graphite arc welder. After welding, capsules were re-weighed and if no significant weight loss occurred (difference < 0.0004 g), they were left in an oven for a few hours at 100°C, to ensure homogeneous H₂O distribution. In all charges the H₂O+CO₂ mass and fluid/silicate ratio were kept constant (3 ± 0.5 mg of H₂O+CO₂, and 30 mg silicate). We

have explored various starting $\text{H}_2\text{O}/\text{CO}_2$ ratios at a given T-P conditions: $\text{XH}_2\text{O}_{\text{in}}$, defined as the $\text{H}_2\text{O}/(\text{H}_2\text{O}+\text{CO}_2)$ molar ratio, was varied in the range 1-0.48 (Table 2). For each run, one capsule containing a Ni-Pd-O alloy sensor, prepared following the procedure of Taylor et al. (1992), was added to monitor the $f\text{H}_2$ during the experiment. A typical run consisted of loading the vessel with six capsules (each with the same starting material but different $\text{XH}_2\text{O}_{\text{in}}$) and the Ni-Pd-O sensor capsule, all of them experiencing the same T-P- $f\text{H}_2$ conditions (Table 2).

Depending on pressure and temperature, the run duration varied between 7 and 18 days (Table 2). Runs were terminated by first using the drop quench device and then switching off the power supply. After the experiment, capsules were checked for leaks, opened, and half of the run product was mounted with epoxy resin and polished for optical observation, and subsequent EMP and SEM analyses. The same procedure was followed for the capsules containing the metallic sensors and the subsequent EMP analysis of the metallic pellet allowed the determination of the $f\text{O}_2$ of the system (Pownceby and O'Neill, 1994; see below).

4.2.2. Water content, $f\text{H}_2$, $f\text{O}_2$ in the capsules

The use of different mixtures of $\text{H}_2\text{O}+\text{CO}_2$ in the capsules allowed us to explore different water fugacities, hence, different melt H_2O content in the experiments (Table 2). In experiments conducted at 900°C and at H_2O -saturated conditions, the size of glass pools was large enough for determining the amount of dissolved water by Fourier transform infra-red (FTIR) spectroscopy. The composition of the natural phonolite resembles that used by Carroll and Blank (1997) for determining the solubility of water in phonolitic melts. Thus, we have used the same analytical conditions and parameters (e.g., extinction coefficients ϵ_{5200} ϵ_{4500}) to determine the water concentration in the glass (Table 3). The small size of the glass pools in experiments run at $850\text{-}800^\circ\text{C}$ did not allow for water determination using FTIR. In such cases, we have calculated the water content of the experimental charges by using the H_2O solubility model of Papale et al. (2006).

Once the water content of the glass in H_2O -saturated charges is known, the water content of charges held at the same temperature and pressure but at $\text{XH}_2\text{O}_{\text{in}} < 1$, was calculated by multiplying the water content determined at H_2O -saturated conditions by the initial mole fraction of water loaded in the capsule ($\text{XH}_2\text{O}_{\text{in}}$, Table 2).

We used the Ni-Pd-O sensors from successful runs to determine the prevailing $f\text{H}_2$. The $f\text{O}_2$ was then determined by using the dissociation constant of water (Robie et al., 1979) and knowing the $f\text{H}_2\text{O}$ at the experimental temperature and pressure. The $f\text{H}_2\text{O}$ was calculated as $f\text{H}_2\text{O} = X\text{H}_2\text{O}_{\text{in}} * f\text{H}_2\text{O}^{\circ}$ where $f\text{H}_2\text{O}^{\circ}$ is the fugacity of pure water (in bars) at the running temperature and pressure (Burnham et al., 1969). In experiments where the sensors failed, the $f\text{H}_2$ was determined using an empirical calibration curve between the H_2 pressure added to the autoclave at room temperature and the $f\text{H}_2$ retrieved from runs in which the sensor was successful (Table 2).

The experiments were conducted at oxygen fugacities around $\text{NNO} \pm 0.5$. However, as $f\text{O}_2$ varies with decreasing activity of water in the melt [$a\text{H}_2\text{O}$, (or $X\text{H}_2\text{O}_{\text{in}}$ in the ideal approximation and neglecting the amount of water dissolved in the melt)] at fixed T, P, $f\text{H}_2$ (e.g., Scaillet et al., 1995; Freise et al., 2009; Andújar and Scaillet, 2012a), water-undersaturated experiments were effectively run at somewhat lower $f\text{O}_2$ ($\text{NNO} - 1 \pm 0.5$ log units ; Table 2). We have also conducted experiments at 850°C and 100 MPa and at an $f\text{O}_2$ 1 log unit lower than the average conditions so as to determine the effects of $f\text{O}_2$ on phase relationships.

4.2.3. Analytical techniques

Phase compositions were determined using a Cameca SX-50 electron microprobe with an accelerating voltage of 15 kV, sample current of 6 nA, and a counting time of 10 s. A defocused beam of 10 μm was used for glasses and a focused beam for minerals. Alkali migration was corrected by using secondary phonolitic standards with a composition similar to the natural obsidian and with known dissolved water contents of 10 wt%, 6 wt% and 1.5 wt% respectively (Andújar et al., 2008, 2010). Mass-balance calculations were used to obtain the phase proportions of the charges using the bulk composition of the starting material and the composition the phases (Table 2).

Experiments conducted at 900°C and 850°C had small crystals (< 10-5 μm) which did not allow to obtain EMP analyses free of glass contamination (i.e.; clinopyroxene with K_2O higher than 0.1 wt%, see below). The glass contribution was removed by subtracting different amounts of glass until the mineral analysis agreed with the corresponding structural formula. We were able to use SEM-EDS to identify all minerals present: alkali feldspar, biotite, magnetite, ilmenite, clinopyroxene and titanite. Whenever possible, at least 5 analyses per phase were done.

4.2.4. Attainment of equilibrium

The crystallization experiments show textural and compositional features similar to those observed in crystallization experiments conducted on phonolitic compositions (e.g., Freise et al., 2003; Scaillet et al., 2008; Andújar et al., 2008, 2010; Fig. 2b). These features include: (1) a homogeneous distribution of the phases within the charges, (2) euhedral crystals, (3) homogeneous phase compositions, including glass (Fig. 2), and (4) the smooth variation of phase proportions and compositions with changes in experimental conditions. The duration of our experiments (1 to 2 weeks) is within the range of that applied in other studies, including for phonolitic systems (Berndt et al., 2001; Freise et al., 2003; Harms et al., 2004; Scaillet et al., 2008), for which close to equilibrium conditions were also proposed (see also Scaillet and Evans 1999; Costa et al., 2004; Andújar et al., 2008, 2010, and Pichavant et al., 2007).

5. Experimental results

5.1. Phase relations

The main features of the phase relations are shown in a series of polybaric-isothermal (Fig. 4a-c) or isobaric-polythermal (Fig. 4d) sections. At 900°C the liquidus phase is biotite at all investigated pressures and melt water content (H_2O_{melt}). Biotite crystallization is followed by the co-crystallization of magnetite plus ilmenite, then alkali feldspar with decreasing H_2O_{melt} . Clinopyroxene has a narrow stability field and only appears at $H_2O_{\text{melt}} < 2.5$ wt% at 900 °C. At about 850°C, magnetite and ilmenite become the liquidus phases and biotite co-crystallization occurs at $H_2O_{\text{melt}} < 6$ wt% (Fig. 4). At 850 °C the stabilities of alkali feldspar and clinopyroxene increase towards higher H_2O_{melt} (between 4 and 5 wt%). At 800 °C major phase changes occur, with co-crystallization of magnetite, clinopyroxene and biotite at liquidus conditions. Alkali feldspar is less affected and still crystallizes for a H_2O_{melt} of 5 wt%, similar to conditions at 850°C. At 800°C, ilmenite disappears and is replaced by titanite. The stability field of titanite is poorly constrained but the results show that under the T- fO_2 conditions explored it only appears at >150 MPa (Figs. 4c and 4d).

Despite the small fO_2 range that we have investigated we find significant changes in phase stabilities with fO_2 . A decrease from NNO to NNO-0.5 at 850°C and 100 MPa, increases the clinopyroxene stability to slightly higher H_2O_{melt} (from 4 wt% at NNO to

4.6 wt% at NNO-0.5) and moves the alkali feldspar field towards lower H_2O_{melt} (Fig. 4, Table 2).

5.2. Phase proportions

Calculated phase proportions show that, as expected, crystallinity increases with decreasing temperature, decreasing H_2O_{melt} and increasing pressure (Fig. 4, Table 2). At 900°C the crystal content is < 5 wt% for H_2O_{melt} between 6 and 3 wt%, at all studied pressures. For H_2O_{melt} of about 1 to 3 wt% the crystal content increases to > 30 wt%. At 850°C and H_2O_{melt} in the range 6.5 - 5 wt% the crystal contents are < 5 wt%, but crystallinities increase to up to 30 wt% when H_2O_{melt} decreases to about 1 wt% (between 200 and 100 MPa). The abrupt and strong increase in crystallinity is enhanced at 50 MPa, where small variations in H_2O_{melt} (± 0.5 wt%) increase the crystal content by about 10 wt%. Charges run at 800°C, 200 MPa, and close to water saturation conditions have crystal contents of 5 wt%, increasing up to 25 wt% when H_2O_{melt} decreases by only 0.5 wt%. Moreover, at such temperature and for a given H_2O_{melt} , a decrease in pressure from 200 to 100 MPa increases the crystal content by about 15 wt%. The large changes in crystallinities with varying H_2O_{melt} are essentially controlled by the amounts of alkali feldspar, whereas in charges with low crystal content (< 5 wt%) biotite, magnetite and ilmenite are the main crystallizing phases (Fig. 4, Table 2).

5.3. Mineral compositions

5.3.1. Ilmenite and magnetite

Ilmenite and magnetite were identified by SEM-EDS but they were often too small for reliable electron microprobe analysis to be performed. We nevertheless analysed Fe-Ti oxides in 7 charges, whose compositions have been corrected out from the glass contribution (less than 3 % of contamination) and the results are shown in Table 4. Magnetite FeO^* and TiO_2 contents range between 77-79 wt%, and 17-14 wt%, respectively, with an Mg# of 3-4. Ilmenite crystallizing at 850°C and at H_2O_{melt} 4-5 wt% has TiO_2 contents in the range 49-51 wt%, while its FeO^* varies from 45 to 42 wt%, depending on H_2O_{melt} (Table 4).

5.3.2. Biotite

Experimental biotites have Mg# in the range 50-68, and define two populations depending on temperature (Fig. 5; Table 4): those from 900°C have higher Mg# (> 57) than at 850°C. At constant pressure and temperature, a decrease in H₂O_{melt} decreases Mg#. For example, at 900°C and 50 MPa the Mg# decreases from 68 to 63 with a decrease in melt water content of only 0.7 wt%. Similar variations in Mg# are observed at 900°C, 100MPa but, over a wider range of H₂O_{melt} (Fig. 5). Otherwise, a decrease of pressure at a constant temperature and H₂O_{melt} increases the Mg# of biotite.

5.3.3. Clinopyroxene

Experimental clinopyroxenes are diopside and hedenbergite according to Morimoto (1989), spanning the range of compositions between En₂₄ Fs₂₆ Wo₄₇ and En₃₄ Fs₁₉ Wo₄₅, with Mg# varying between 47 and 64. Clinopyroxene composition is affected by variations in experimental temperature and changes in melt water content (Fig.6).

When temperature increases from 800 to 850°C, the Mg# of clinopyroxene increases from 45 to 55, the En content from 24% to 29%, whilst Fs decreases from 27% to 23%, and Wo remains almost constant. These variations include charges ran at different P and *f*O₂. At pressures ≥ 100 MPa a variation in H₂O_{melt} does not appreciably affect clinopyroxene composition, but in runs at 50 MPa, as H₂O_{melt} increases, the En and Mg# increase while Fs and Wo decrease (Fig. 6). Similar compositional variations were observed in experiments done on other phonolites (e.g., Andújar et al. 2008, 2010) but, their magnitude remain smaller compared to those observed in more silicic compositions (e.g., Scaillet and Evans, 1999).

5.3.4. Alkali feldspar

Alkali feldspars are anorthoclase with compositions between An₉ Ab₇₀ Or₂₁ and An₂ Ab₆₄ Or₃₄, depending essentially on temperature and H₂O_{melt}. At constant pressure, both An and Ab decrease whereas Or increases with decreasing temperature and H₂O_{melt} (Fig. 7). However, the effect of temperature is larger than the effect of H₂O_{melt} and the compositional variations are enhanced at lower pressures. For example, at 50 MPa and for a constant H₂O_{melt} of 2 wt%, an increase in temperature from 850°C to 900°C increases the An content of anorthoclase from 2 mole % to 9 mole%. In contrast, at 200 MPa and constant H₂O_{melt} (4 wt%), a variation in temperature from 850 to 800°C does not appreciably affect the composition of alkali feldspar.

5.4. Glass

Residual glass compositions are reported in Table 5. The $\text{Na}_2\text{O}+\text{K}_2\text{O}$ is between 15 and 18 wt%, and SiO_2 contents range between 61.7 and 58.3 wt% (reported compositions were re-calculated to 100% anhydrous; Table 5; Fig. 8). According to Le Maitre et al. (1989), all experimental glasses are phonolitic and mildly per-alkaline (molar $\text{Na}+\text{K}/\text{Al}$ between 1.1 and 1.3). The glass composition varies according to changes in intensive parameters and thus with phase proportions. For a given pressure and temperature, SiO_2 displays a complex trend of increase and then decrease with decreasing $\text{H}_2\text{O}_{\text{melt}}$ (Fig 8a). For a constant temperature, the highest SiO_2 enrichment is displaced towards higher $\text{H}_2\text{O}_{\text{melt}}$ with increasing pressure, though the effect is more pronounced at $< 900^\circ\text{C}$ (Fig. 8). The SiO_2 variation is controlled by the onset of alkali feldspar crystallization, although the maximum SiO_2 enrichment depends also on the relative abundances of oxides and biotite (Table 2). Glasses from charges at 200 MPa and 900°C with biotite present have slightly lower SiO_2 (60.5 wt%) than at 850°C (61.5 wt%), where magnetite-ilmenite prevail over biotite (Figs.4 and 8). At a given $\text{H}_2\text{O}_{\text{melt}}$, the SiO_2 content increases by about 0.5-1 wt% with an increase of 50°C and of 50 MPa.

A decrease in temperature of 50°C at a given pressure and $\text{H}_2\text{O}_{\text{melt}}$, leads to a decrease of TiO_2 , MgO and CaO contents by about 50% relative, whereas both Na_2O and K_2O slightly increase. A decrease in pressure leads to an increase in MgO and a decrease in CaO contents. However, at 50 MPa, compositional changes with intensive variables are different from those observed at higher pressures. Residual glasses at 900°C have higher MgO contents than at 850°C . Moreover, a decrease in $\text{H}_2\text{O}_{\text{melt}}$ increases the MgO content of the glass. Such compositional variations have been also documented in other experiments performed on similar compositions at low pressure (e.g., Andújar and Scaillet, 2012a). The effect of $f\text{O}_2$ on glass compositions is small, reflecting the limited range of $f\text{O}_2$ investigated. However, experiments conducted at more reducing conditions (NNO-2) yield glasses with lower TiO_2 , MgO and CaO and higher SiO_2 , Al_2O_3 and K_2O contents than those synthesised at NNO.

6. Discussion

6.1. Natural versus experimental data: constraints on the pre-eruptive conditions of Roques Blancos

The comparison between the mineral assemblage of the natural phonolite (14 wt % of phenocrysts, mainly alkali feldspar, but also clinopyroxene, biotite and Fe-Ti oxides) and those from experiments provides first-order constraints on the magma pre-eruptive conditions. At temperatures between 850 and 900°C the crystal content and phase assemblage of the natural phonolite have been reproduced at pressures between 75 and 25 MPa, and H_2O_{melt} 2.0-4.0 wt% (Fig. 4). Lower temperatures (e.g. 800 °C) can be ruled out because of the much higher crystal content and absence of ilmenite in the explored ranges of H_2O_{melt} and pressures. Pressures higher than about 75 MPa can also be ruled out because clinopyroxene only occurs at crystal contents higher than in the natural phonolite. We have not performed experiments at < 50 MPa, but extrapolation of the crystallinity and phase equilibrium relationships obtained at 50 MPa also suggests much higher crystallinities at pressures significantly lower than 50 MPa. To refine and test the robustness of such constraints we use below the compositions of mineral and glass.

Natural magnetite has a Mg# of 5 whereas our two experimental magnetites from experiments conducted at 850°C, 100 and 50 MPa, and H_2O_{melt} of about 3 wt% have Mg# of 3 to 4. Magnetite composition varies with temperature and fO_2 (e.g. Andújar et al. 2008, 2010) and thus, the slightly higher Mg# of the natural magnetite suggests higher temperatures (e.g., > 850°C) or/and more oxidizing conditions (e.g., $fO_2 > \text{NNO}$). We have reproduced the TiO_2 content of the natural ilmenite at 850°C, 200 MPa and H_2O_{melt} of 5.5 wt%, although these conditions are different from those inferred above.

Experimental biotites crystallizing between 50 and 200 MPa at 900°C, and H_2O_{melt} between 1.5-4.5 wt% encompass the Mg# of natural biotites (Mg# 63, Fig. 5). However, at this temperature only experiments performed at 50 MPa and $H_2O_{\text{melt}} < 2.5$ wt% reproduce the phase assemblage and crystal content of the natural phonolite. At 850°C the experimental biotites have lower Mg# than those from the phonolite.

We have successfully reproduced the rim and core compositions of the natural alkali feldspars. Their Ca-rich rims (An_{7-8}) are reproduced at 900°C, 50 MPa and $H_2O_{\text{melt}} \sim 2$ wt% while cores (the bulk of crystals, see Fig 3), which range from $An_{2.5}$ to An_4 , are reproduced at 850°C, 50 MPa and H_2O_{melt} between 2-3 wt% (Fig. 7). These results support our pressure estimate of 50 MPa for the storage conditions prior to eruption but indicate also that crystallization of natural feldspars occurred at two different conditions: the Ca-poor cores crystallized at 850°C, whilst the Ca-rich rim crystallized

at 900°C. Such a temperature difference suggests a change in the storage temperature of the reservoir just prior to eruption which, as we show below, is also consistent with biotite and Fe-Ti oxide reequilibration.

We have not obtained EMP analyses of clinopyroxene in charges produced at 900°C due to the small size of crystals; however, the compositional trends displayed by the experimental clinopyroxenes support this temperature for natural clinopyroxene crystallization. At 850°C, 50 MPa and H_2O_{melt} of 2 wt%, both the Mg# and En content of natural clinopyroxene are closely reproduced yet, Fs and Wo are slightly different. However, an increase of temperature of 50°C will produce a 5% moles increase in the En content and Mg# of clinopyroxenes but also, a 5% moles decrease in the Fs content, producing a clinopyroxene similar to the natural one (Fig.6; see previous section).

The comparison between natural and experimental phase relationships and mineral compositions therefore suggests pre-eruptive conditions for the Roques Blancos phonolite to be 850-900°C, 50 MPa, and melt water contents between 2 to 2.5 wt% ($P_{\text{total}} < P_{H_2O}$). At such conditions the SiO_2 , CaO, Na_2O , MgO, TiO_2 and K_2O contents of the residual melt are closely reproduced (Table 1; Fig. 8). Only FeO^* and Al_2O_3 contents are different (but almost within error if analytical uncertainties are considered) than those from experiments conducted at 850-900°C and 50 MPa (Fig. 8).

We do not have enough experimental data from different fO_2 (i.e., biotite, Fe-Ti oxides) to make a precise determination of the pre-eruptive oxygen fugacity. However, the fact that we have successfully reproduced the phase assemblage, crystal content and phase compositions of the natural phonolite at an $fO_2 \sim NNO$ suggests that such an fO_2 broadly prevailed in the reservoir. Moreover, the Mg# of the natural biotite (which is highly sensitive to fO_2) is reproduced at an $fO_2 \sim NNO-1$; hence a pre-eruptive fO_2 between NNO and NNO-1 appears to be a good redox estimate for the natural phonolite, in accord with constraints obtained from natural magnetite-ilmenite pairs (Table 1) and with those obtained previously for other phonolites from Tenerife (Ablay et al., 1998; Andújar et al., 2008, 2010; Andújar and Scaillet, 2012a). On the basis of the foregoing discussion we conclude that prior to eruption the Roques Blancos phonolite was stored at 50 ± 15 MPa, $875^\circ\text{C} \pm 25^\circ\text{C}$, with H_2O_{melt} 2-2.5 wt%, at an fO_2 of NNO-0.5 (± 0.5). Although the pre-eruptive H_2O_{melt} is rather low, the low pressure of magma storage implies that any coexisting fluid phase in the reservoir will be dominated by H_2O (ie $X_{H_2O} > 0.5$). Evidence for dissolved pre-eruptive CO_2 is generally lacking in phonolite magmas (e.g., Andujar and Scaillet, 2012a,b), including at Tenerife, which

shows that, if present, CO₂ must reside primarily in the vapor phase, albeit in moderate amounts to be compatible with our inferred H₂O_{melt}.

6.2. Evidence for late magma reheating upon mixing before eruption

Many Roques Blancos alkali feldspars are characterised by a reverse compositional zoning with An-rich rims and Or-poor cores (Fig. 3). We have successfully reproduced such An-rich compositions at 900°C, 50 MPa, 2 wt% H₂O_{melt} whereas cores are reproduced at the same pressure and H₂O_{melt} but at a lower T, 850°C (Figs. 4 and 7). Reverse zoning in feldspars are generally interpreted as arising from crystallisation of a more Ca-rich melt, often related to mixing with a more mafic magma (e.g., Couch et al. 2001, Martel et al, 2006). Alternatively, experimental works have shown that such Ca-rich rims can be also produced by increasing temperature without interaction with a mafic body (e.g., Rutherford et al., 1985; Couch et al., 2001), by increasing pressure at water-saturated conditions (Rutherford and Devine 2008), or by an increase in water activity via the preferential loss of a CO₂ (Holloway, 1976). To discriminate between the different possibilities, it is useful to compare changes in An content with changes in other minor elements as shown by Triebold et al. (2006) and Ruprecht and Wörner (2007). These authors suggest that a process of magma mixing can be identified in feldspars when the An enrichment is accompanied by an increase in Fe content whereas when Fe remains constant, only an increase in temperature can explain the Ca-rich compositions. The compositional traverses show that the increase in the An content towards the rims of the crystals is indeed coupled with an increase in the FeO*, TiO₂ and BaO which suggests that such Ca-rich rims record the income of a more mafic and higher temperature melt, as proposed by Triebold et al. (2006) and Ruprecht and Wörner (2007). This hypothesis is also supported by our experimental results: the observed CaO-FeO*-TiO₂ enrichment of the alkali feldspar rims cannot be explained only by a single shift in temperature or water activity because in each case, the stability field, phase proportions and composition of phases like biotite, magnetite, or clinopyroxene will be also modified. In detail, at 900°C for reproducing the low Ca-cores of feldspars, crystal contents > 30 wt% and H₂O_{melt} <1.7 wt% are required (fig. 4). Then, to generate the An₇₋₈ rims, H₂O_{melt} should increase to 2.5 wt% and the crystal content should be reduced by ~50% to achieve the 14 wt% phenocryst of the phonolite (Fig. 4). The presence of resorbed textures in feldspars cores and clinopyroxenes (Fig. 3) is compatible with such an hypothesis; however, although the rise in temperature or

H_2O_{melt} will increase the Ca content of the coexisting melt, producing a shift in the An content, it will keep FeO^* and TiO_2 concentrations constant, a trend unlike the rimward enrichment in these elements observed in natural feldspars (Fig. 8). The above lines of evidence thus suggest that the most likely mechanism for explaining the compositional zonation of alkali feldspars is mixing with a hotter and more mafic magma. In such a scenario, the observation that only biotite and Fe-Ti oxides compositions record the conditions following the intrusion of the more mafic and hotter melt can be explained by their much faster kinetics of intracrystalline diffusion compared to other minerals (e.g., Cherniak and Dimanov, 2010; Van Orman and Crispin, 2010). Although we do not have detailed compositional zoning in clinopyroxene to further check this hypothesis, the BSE images show multiple growth zones with dissolution surfaces, which is consistent with an open-system evolution with abrupt changes in temperature and composition.

Magma mixing and mingling are common processes occurring at Tenerife, as recorded by the existence of mingled-mixed products or by reversely zoned phenocrysts (Araña et al., 1994; Ablay et al., 1998; Neumann et al., 1999, Triebold et al, 2006), as discussed above. The steep increase in Ba recorded in the alkali feldspars (Fig. 3) provides insights into the composition of the mafic end-member. According to Ablay et al. (1998), among the mafic magmas erupted in the last 30 kyr, tephriphonolites are the most Ba-enriched, in particular those erupted from Pico Viejo vent, which can contain up to 1400 ppm of Ba. Estimated pre-eruptive temperatures of such tephriphonolites are in the range 1020-1040°C (Ablay et al., 1998; Neumann et al., 1999), hence they are hot enough to increase temperature, at least locally, yielding Ca-rich overgrowth on alkali feldspars of the Roques Blancos phonolite when entering in the reservoir, although in detail the thermal effects will depend on the relative masses of juxtaposed magmas.

According to these observations, the following sequence of events for the late magmatic evolution of the Roques Blancos magma reservoir prior to the eruption can be proposed. The phonolite was ponding at depths between 1-2 km and at temperatures around 850°C, where the bulk of crystallization of the alkali feldspars occurred yielding the Ca and Ba poor cores. Intrusion of a hotter tephriphonolitic melt into the more evolved magma increased the temperature of the resident phonolite and enriched the residual melt in Ca, Ti, Fe and Ba from which the outer rims of feldspar crystallized, while biotite and Fe-Ti oxides quickly re-equilibrated. The arrival of this hotter and

more mafic intrusion might have triggered the eruption some time later (e.g., Folch and Martí, 1998).

6.3. Central versus flank eruptions in Tenerife and their relation to different eruptive styles

The volcanic activity of the last 30 kyr of the Teide-Pico Viejo complex is characterised by the eruption of intermediate to phonolitic magmas which volumetrically predominated over the basaltic ones (Ablay et al., 1998; Carracedo et al., 2007, Martí et al., 2008). The phonolitic eruptions alternate between central Pico Teide and Pico Viejo vents and several flank domes located around the stratovolcanoes, with these last dominating the evolution of the actual volcanic system in terms of number of events (Ablay and Martí, 2000; Carracedo and Rodríguez-Badiola, 2006; Rodríguez-Badiola et al., 2006; Carracedo et al., 2007). Flank dome eruptions share several physical, petrographic, geochemical, and volcanological features. Phonolitic domes are located at heights between 2000 and 3000 m a.s.l. over the steep flanks of the Teide-Pico Viejo stratovolcanoes: generally they are volumetrically smaller than eruptions occurring from the central vents (Ablay, 1997; Martí et al., 2008; Carracedo et al., 2007; Martí et al., 2012) and are characterised by the emission of thick phonolitic lava flows. They typically have also an explosive phase that produces significant fall-out deposits, as documented for the eruptions of Montaña Blanca and El Boquerón (Ablay et al. 1995; Andújar and Scaillet, 2012a; García et al., 2012)

Previous estimates of the storage conditions of flank dome eruptions in Tenerife were done using thermo-barometric models (Ablay, 1997; Ablay et al., 1995; Ablay et al., 1998). Coexisting Fe-Ti oxides of Arenas Blancas, Montaña Las Lajas, and Montaña Blanca flank eruptions yield temperatures in the range 775-900°C (Ablay, 1997; Ablay et al., 1995; Ablay et al., 1998). These authors also measured water contents of melt inclusions trapped in clinopyroxenes from Montaña Majua and Montaña Blanca flank dome eruptions, reporting values of 1.2 - 2.5 wt%, and 3 - 4.5 wt%, respectively. Using the volatile content and the water solubility model of Carroll and Blank (1997), Ablay et al. (1995) inferred a storage pressure of 100 MPa for the Montaña Blanca eruption. New experimental results by Andújar and Scaillet (2012a) using the products of the sub-plinian phase of the Montaña Blanca eruption suggest instead that this magma was stored at $850\pm 15^\circ\text{C}$, 50 ± 15 MPa, 2.5 ± 0.5 wt% $\text{H}_2\text{O}_{\text{melt}}$. This phase of the eruption involved the emission of a crystal-poor phonolitic magma (1 to 4 wt% of phenocrysts)

with a composition similar to that of Roques Blancos. We have calculated the magma viscosities of these two phonolites (models of Giordano et al., 2008, and Scaillet et al. 1998; Andújar and Scaillet, 2012b) and have found about the same values ($10^{4.1}$ Pa*s). This and their similar storage conditions, which are close to water-saturation according to available H₂O-solubility models in phonolitic melts (Carroll and Blank, 1997; Schmidt and Behrens, 2008), indicate that both magmas would respond similarly upon decompression. The explosive nature of the Montaña Blanca eruption suggests that it is likely that the beginning of the Roques Blancos eruption had a short-lived highly explosive initial phase, which is in agreement with the recent identification of fall-out deposits associated with this eruption (O. García unpublished data).

The physical and petrological features shared between the most recent satellite phonolitic eruptions of Teide-Pico Viejo (Fig. 1) and that of Montaña Blanca, El Boquerón and Roques Blancos, all point towards a shallow origin for these flank eruptions, which appear to have been fed by reservoirs located at depths of 1-2 km below the surface. These shallow values contrast with those experimentally determined for central eruptions occurring from Teide proper, which were constrained to be about 5 km below the actual summit of Pico Teide volcano (Andújar et al., 2010). In figure 9 we have projected the depths for the Roques Blancos, Montaña Blanca and central Teide phonolitic magmas. It shows that phonolitic magmas can be stored at various depths in Tenerife, up to very close to the surface (~1-2 km below the surface), suggesting that the phonolite storage region of Teide is not characterised by one single and large reservoir, but instead by various isolated, possibly transient, magma pockets that can coexist simultaneously, re-enforcing and supporting previous observations obtained from petrological data and modelling efforts (Ablay et al., 1998; Andújar and Scaillet, 2012a; Martí and Geyer, 2009). The characteristics of the actual plumbing system beneath Teide-Pico Viejo where several phonolitic shallow reservoirs can co-exist, as well as the difference in storage depths, can thus explain the multiple shifts between central and lateral eruptions documented to occur at this stratovolcano (Martí and Geyer, 2009).

7. Conclusions

Crystallization experiments on a phonolitic product of the Roques Blancos eruption, a representative flank eruption of the large Teide stratovolcano, show that it was stored at shallow depths (about 50 MPa or 1-2 km) below the edifice with about 2.5 wt % water dissolved in the melt. The main petrological features (crystal content, phase

assemblage, phase compositions) of the natural phonolite are reproduced at 900°C, though the composition of Ca-poor cores of alkali feldspar record lower temperatures of about 850°C. The zoning pattern of natural alkali feldspars show that they have high Ba, Ti, and Fe rims which, we suggest, record a late and transient reheating following mixing of the resident magma with a more mafic melt. Such shallow and water-rich storage conditions were also determined for another flank and Plinian eruption of Teide and contrast with the deeper reservoir inferred for predominantly effusive eruptions of magmas emitted from the central Teide cone. Such differences in storage depths and locations illustrate the complexity of the magma plumbing system that may currently exist below Teide, which does not appear to be fed from a single large reservoir. Instead, the evidence call for multiple isolated small magma reservoirs, whose level of assembly in upper crust is in part controlled by the feedback existing between the evolution and growth of the aerial cone built/destroyed during eruptions and the local stress field at depth.

The results from the current work should help improve hazard assessment at Tenerife, along with the forecasting the future behaviour of phonolitic magmas stored below Teide-Pico Viejo volcanic system. In particular, the new constraints we provide about both pre-eruptive H_2O_{melt} of phonolites and their storage depths may help in providing a first estimate of the explosive/effusive potential of these magmas by using the location of tremors during an on-going eruption at central parts of the island. Nevertheless, we stress that the explosive vs non-explosive character of alkali-rich magmas can be easily changed by additional factors (ie, influx of other volatile species like CO_2 , degassing, interaction with meteoric water, mixing with mafic compositions within the conduit); and will be always subordinated to the composition of the ascending magma, which is so far virtually impossible to know with the available monitoring tools.

Acknowledgements

J.A. thanks M. Pompilio and A. Burgisser for their scientific discussions that improved previous versions of the manuscript. L. Ramon, O. Rouer and I. Di Carlo are thanked for their technical support. Comments from J.M. Castro greatly helped to improve the manuscript. This work was funded by “Beatriu de Pinós” fellowship BPA-00072 and a fellowship grant from the University of Orléans. Joan Martí is thanked by providing the

logistical support during rock sampling at Tenerife, as well as for the comments and editorial handling of the paper.

References

- Ablay, G. J., Ernst, G. G. J., Martí, J., Sparks, R.S.J., 1995. The 2ka subplinian eruption of Montaña Blanca, Tenerife. *Bull. Volcanol.* 57, 337-355.
- Ablay, G. J., 1997. Evolution of the Teide-Pico Viejo volcanic complex and magmatic system (Tenerife, Canary Islands). Department of Geology. Bristol, University of Bristol. 336 pp.
- Ablay, G. J., Carroll, M.R., Palmer, M.R., Martí, J., Sparks, R.S.J., 1998. Basanite-Phonolite Lineages of the Teide-Pico Viejo Volcanic Complex, Tenerife, Canary Islands. *J. Petrol.* 39, 905-936.
- Ablay, G. J., Martí, J., 2000. Stratigraphy, structure, and volcanic evolution of the Pico Teide-Pico Viejo formation, Tenerife, Canary Islands. *J. Volcanol. Geotherm. Res.* 103, 175-208.
- Andújar, J., Costa, F., Martí, J., Wolff, J.A., Carroll, M.R., 2008. Experimental constraints on pre-eruptive conditions of phonolitic magma from the caldera-forming El Abrigo eruption, Tenerife (Canary islands). *Chem. Geol.* 257, 173-191
- Andújar, J., Costa, F., Martí, J., 2010. Magma storage conditions of the last eruption of Teide volcano (Canary Islands, Spain). *Bull. Volcanol.* 72, 381-395.
- Andújar, J., Scaillet, B., 2012a. Experimental constraints on parameters controlling the difference in the eruptive dynamic of phonolitic magmas: the case from Tenerife (Canary Islands). *J. Petrol.* <http://dx.doi.org/10.1093/petrology/EGS033>
- Andújar, J., Scaillet, B., 2012b. Relationships between pre-eruptive conditions and eruptive styles of phonolite–trachyte magmas. *Lithos* 152, 122-131.
- Araña, V., 1971. Litología y estructura del Edificio Cañadas, Tenerife (Islas Canarias). *Estudios Geologicos* 27, 95-135.
- Araña, V., Martí, J., Aparicio, A., García-Cacho, L., Carcía-García, R., 1994. Magma mixing in alkaline magmas: An example from Tenerife, Canary Islands, *Lithos* 32, 1–19.

- Balcells, R., Hernández-Pacheco, A., 1989. El domo-colada de Roques Blancos. In: Araña, V. and Coello, J. (eds) Los volcanes y la caldera del Parque Nacional del Teide (Tenerife, Islas Canarias). Madrid: ICONA, pp. 235-253.
- Berndt, J., Holtz, F., Koepke, J., 2001. Experimental constraints on storage conditions in the chemically zoned phonolitic magma chamber of the Laacher See volcano. *Contrib. Mineral. Petrol.* 140,469-486.
- Bonaccorso, A., Calvari, S., Coltelli, M., Del Negro, C., and Falsaperla, S. (Eds.), 2004. Mt. Etna: Volcano Laboratory, Geophysical Monograph series vol. 143, 369 PP., ISSN: 0065-8448; ISBN: 0-87590-408-4.
- Burnham, C. W., Holloway, J. R., Davis, N. F., 1969. Thermo-dynamic properties of water to 1000°C and 10 000 bar. *Geol. Soc. Amer. Spec. Pap.* 132, 1–96.
- Carracedo, J. C., Rodríguez-Badiola, E., 2006. Los domos y domos-colada del complejo volcanico del Teide. In: Carracedo, J. C. (ed.) Los volcanes del parque nacional del Teide. Madrid: serie técnica Organización de Parques Nacionales, Ministerio de Medio Ambiente, pp. 213-238.
- Carracedo, J.C., Rodríguez-Badiola, E., Guillou, H., Paterne, M., Scaillet, S., Pérez-Torrado, F. J., Paris, R., Fra-Paolo, U., Hansen, A., 2007. Eruptive and structural history of Teide volcano and rift zones of Tenerife, Canary Islands. *Geol. Soc. Am. Bull.* 119, 1027-1051.
- Carroll, M. R., Blank, J.G., 1997. The solubility of H₂O in phonolitic melts. *Am. Mineral.* 82, 549-556.
- Cherniak, D. J., Dimanov, A., 2010. Diffusion in Pyroxene, Mica and Amphibole *Rev. Mineral. Geochem.* 72, 641-690.
- Corsaro, R.A., Miraglia, L., Pompilio, M., 2007. Petrologic evidence of a complex plumbing system feeding the July-August 2001 eruption of Mt. Etna, Sicily, Italy. *Bulletin of Volcanology* 69, 401-421.
- Costa, F., Scaillet, B., Pichavant, M., 2004. Petrological and experimental constraints on the Pre-eruption conditions of Holocene dacite from Volcán San Pedro (36°S, Chilean Andes) and the importance of sulphur in silicic subduction-related magmas. *J. Petrol.* 45, 855-881.
- Couch, S., Sparks, R.S.J., Carroll, M.R., 2001. Mineral disequilibrium in lavas explained by convective self-mixing in open magma chamber. *Nature* 411,1037-1039.

- Deer, W.A.; Howie, R.A., Zussman, J., 1972. Rock forming minerals: Framework silicates 4, 435 pp.
- Di Carlo, I., Pichavant, M., Rotolo, S.G., Scaillet, B., 2006. Experimental crystallization of a High-K arc basalt: the golden pumice, Stromboli volcano (Italy). *J. Petrol.* 47, 1317-1343.
- Freise, M., Holtz, F., Nowak, M., Scoates J.S., Strauss, H., 2009. Differentiation and crystallization conditions of basalts from the Kerguelen large igneous province: an experimental study . *Contrib. Mineral. Petrol.* 158, 505–527.
- Freise, M., Holtz, F., Koepke, J., Scoates, J., Leyrit, H., 2003. Experimental constraints on the storage conditions of phonolites from kerguelen Archipelago. *Contrib. Mineral. Petrol.* 145, 659-672.
- Folch, A., Martí, J., 1999. The generation of overpressure in felsic magma chambers by replenishment. *Earth Planet. Sci. Lett.* 163, 301-314.
- García, O., Bonadonna, C., Martí, J., Pioli, L., 2012. The 5,660 yr BP boquerón explosive eruption, Teide-Pico Viejo complex, Tenerife. *Bull. Volcanol.* DOI. 10.1007/s00445-012-0646-5
- Harms, E., Gardner, J.E., Schmincke, H.U., 2004. Phase equilibria of the lower Laacher See Tephra (East Eifel, Germany): constraints on pre-eruptive storage conditions of a phonolitic magma reservoir. *J. Volcanol. Geotherm. Res.* 134, 135-148.
- Holloway, J.R., 1976. Fluids in the evolution of granitic magmas: consequences of finite CO₂ solubility. *Geol. Soc. Am. Bull.* 87, 1513-1518.
- Kahl, M., Chakraborty, S., Costa, F, Pompilio, M., 2011. Dynamic plumbing system beneath volcanoes revealed by kinetic modeling, and the connection to monitoring data: An example from Mt. Etna. *Earth. Planet. Sci. Lett.* 308, 11-22.
- Le Maitre, R.W., Bateman, P., Dudek, A., Keller, J., La Meyre Le Bas, M.J., Sabine, P.A., Schmid, R., Sorensen, H., Streckeisen, A., Wooley, A.R., Zanettin, B., 1989. A classification of igneous rocks and glossary of terms. Blackwell Scientific Publications, 193 pp. Oxford.
- Martel, C., Pichavant, M., Holtz, F., Scaillet, B., 1999. Effects of fO_2 and H₂O on andesite phase relations between 2 and 4 kbar. *J. Geophys. Res.* 104, 29,453-29,470.
- Martel, C., Ali, A.R., Poussineau, S., Gourgaud, A., Pichavant, M., 2006. Basalt-inherited microlites in silicic magmas: Evidence from Mount Pelée (Martinique, French West Indies). *Geology* 34, 905-908.

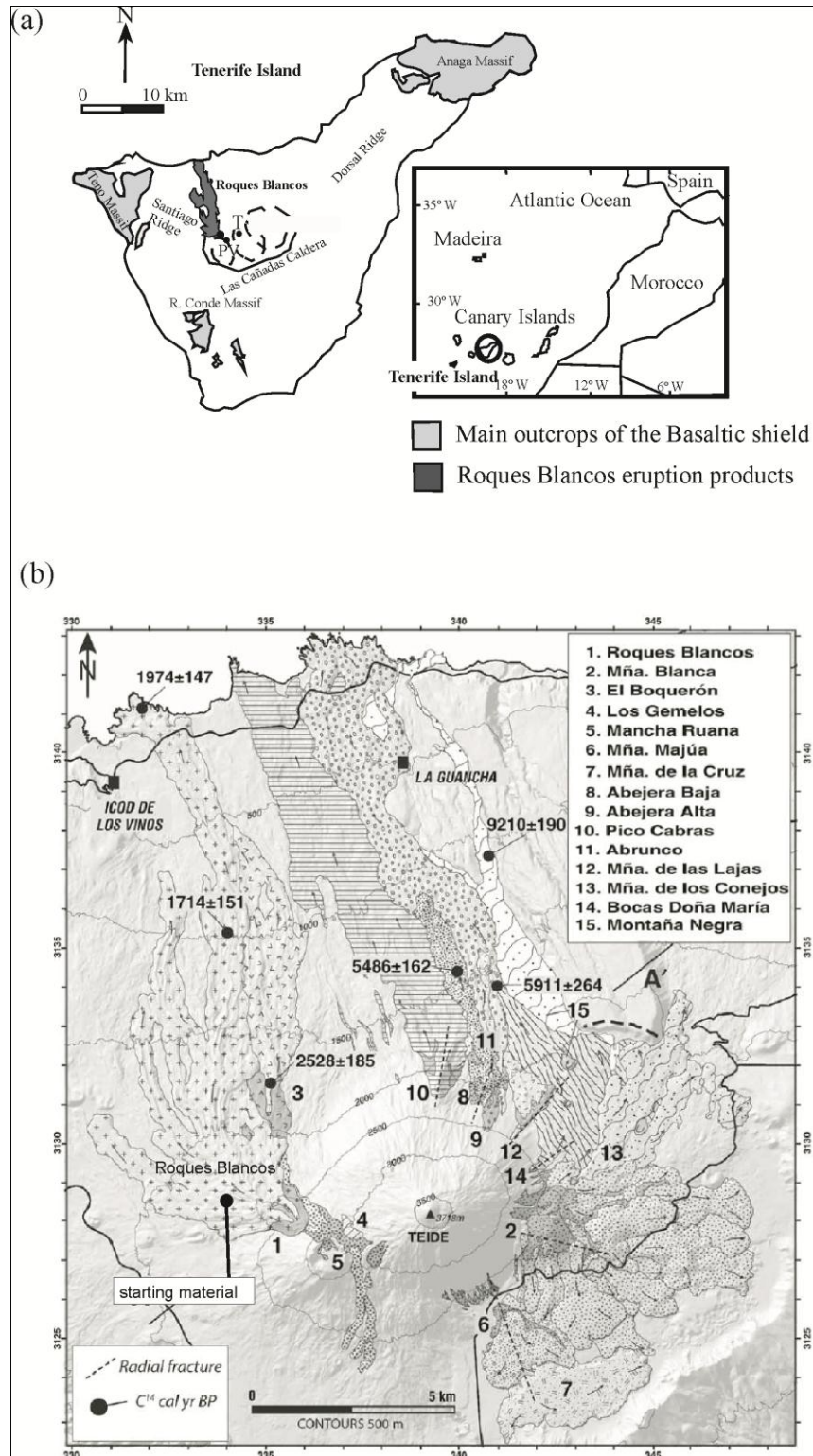
- Martí J., Mitjavila J., Araña, V., 1994. Stratigraphy, structure and geochronology of the Las Cañadas caldera (Tenerife, Canary Island). *Geol. Mag.* 131,715-727.
- Martí, J., Gudmundsson, A., 2000. The Las Cañadas caldera (Tenerife, Canary Islands): an overlapping collapse caldera generated by magma-chamber migration. *J. Volcanol. Geotherm. Res.* 103, 161-173.
- Martí, J., Geyer, A., Andújar, J., Teixidó, F., Costa, F., 2008. Assessing the potential for future explosive activity from Teide-Pico Viejo. *J. Volcanol. Geotherm. Res.* 178, 529-542.
- Martí, J., Geyer, A., 2009. Central vs flank eruptions at Teide–Pico Viejo twin stratovolcanoes (Tenerife, Canary Islands). *J. Volcanol. Geotherm. Res.* 181, 47-60.
- Martí, J., Sobradelo, S., Felpeto, A., García, O., 2012. Eruptive scenarios of phonolitic volcanism at Teide-Pico Viejo volcanic complex (Tenerife, Canary Islands). *Bull. Volcanol.* 74, 767-782.
- Morimoto, N., 1989. Nomenclature of pyroxenes. Subcomitee on pyroxenes. Commission on new minerals and mineral names. *Can. Mineral.* 27, 143-156.
- Neumann, E.-R., Wulff-Pedersen, E., Simonsen, S.L., Pearson, N.J., Martí, J., Mitjavila, J., 1999. Evidence for fractional crystallization of periodically refilled magma chambers in Tenerife, Canary Islands. *J. Petrol.* 40, 1089-1123.
- Papale P, Moretti R, Barbato, D., 2006 The compositional dependence of the saturation surface of H₂O + CO₂ fluids in silicate melts. *Chem. Geol.* 229, 78-95.
- Pichavant, M., Costa, F., Burgisser, A., Scaillet, B., Martel, C , Poussineau, S., 2007. Equilibration scales in silicic to intermediate magmas - Implications for phase equilibrium studies. *J. Petrol.* 48, 1955-1972
- Pownceby, M.I., O'Neill, H. St.C., 1994. Thermodynamic data redox reactions at high temperatures.III. Activity-composition relations in Ni-Pd alloys from EMF measurements at 850-1250 K and calibration of the NiO+Ni-Pd assemblage a redox sensor. *Contrib. Mineral. Petrol.* 116, 327-339.
- Robie, R.A., Hemingway, B.S., Fisher, J.R., 1979. Thermodynamic properties of minerals and related substances at 298.15 K and 1 bar (10⁵ pascals) pressure and at higher temperatures. *U.S. Geol. Surv. Bull.* 1452, 456.
- Rodríguez Badiola, E., Pérez Torrado, F.J., Carracedo, J.C., Guillou, H., 2006. Petrografía y geoquímica del edificio volcánico Teide-Pico Viejo y las dorsales

- noreste y noroeste de Tenerife, in Carracedo, J.C., ed., Los Volcanes del Parque Nacional del Teide: Madrid, Serie Técnica. Publicación Organismo Autónomo Parques Nacionales, Ministerio de Medio Ambiente, p. 129–188.
- Ruprecht, P., Wörner, G., 2007. Variable regimes in magma systems documented in plagioclase zoning patterns: El Misti stratovolcano and Andahua monogenetic cones. *J. Volcanol. Geotherm. Res.* 165, 142-162.
- Rutherford, M.J., Sigurdson, H., Carey, S., Davis, A., 1985. The May 18, 1980, eruption of Mount St. Helens 1. melts composition and experimental phase equilibria. *J. Geophys. Res.* 90, 2929-2947.
- Rutherford, M.J., Devine, J.D. III, 2008. Magmatic conditions and processes in the storage zone of the 2004-2006 Mount St. Helens dacite. In: A volcano Rekindled: the renewed eruption of Mount St. Helens 2004-2006. Sherrod, D.R., Scott, W.E., Stauffer, P.H. (eds). U.S. Geol Surv. Prof Paper pp.17-50.
- Sauerzapf, U., Lattard, D., Burchard, M., Engelmann, R., 2008. The titanomagnetite-ilmenite equilibrium: New experimental data and thermo-oxybarometric application to the crystallization of basic to intermediate rocks. *J. Petrol.* 49, 1161-1185.
- Scaillet, B., Pichavant, M., Roux, J., Humbert, G., Lefevre, A. (1992).
- Scaillet, B., Pichavant, M., Roux, J., 1995. Experimental crystallization of leucogranite magmas. *J. Petrol.* 36, 663-705.
- Scaillet, B., Holtz, F., Pichavant, M., 1998. Phase equilibrium constraints on the viscosity of silicic magmas 1. Volcanic-plutonic comparison. *J. Geophys. Res.* 103, 27,257-27,266.
- Scaillet, B., Evans, B.W., 1999. The 15 June 1991 eruption of Mount Pinatubo. I. phase equilibria and Pre-eruption P-T- f_{O_2} - a_{H_2O} . *J. Petrol.* 40, 381-411.
- Scaillet, B., Pichavant, M., Cioni, R., 2008. Upward migration of Vesuvius magma chamber over the past 20,000 years. *Nature* 455, 216-219.
- Schmidt, B.C., Behrens, H., 2008. Water solubility in phonolite melts: influence of melt composition and temperature. *Chem. Geol.* 256, 259–268.
- Taylor, J.R., Wall, V.J. & Pownceby, M.I. (1992). The calibration and application of accurate redox sensors. *American Mineralogist* 77, 284-295.
- Triebold, S., Kronz, A., Wörner, G., 2006. Anorthite-calibrated backscattered electron profiles, trace elements, and growth textures in feldspars from the Teide-Pico viejo volcanic complex (Tenerife). *J. Volcanol. Geotherm. Res.* 154, 117-130.

Van Orman, J., Crispin, K.L., 2010. Diffusion in Oxides. *Rev. Mineral. Geochem.* 72, 757 - 826

Wiesmaier, S., Troll, V.R., Carracedo, J.C., Ellam, R.M., Bindeman, Y., Wolff, J.A., 2012. Bimodality of Lavas in the Teide-Pico Viejo Succession in Tenerife—the Role of Crustal Melting in the Origin of Recent Phonolites. *J. Petrol.*
doi:10.1093/petrology/egs056

Figure captions



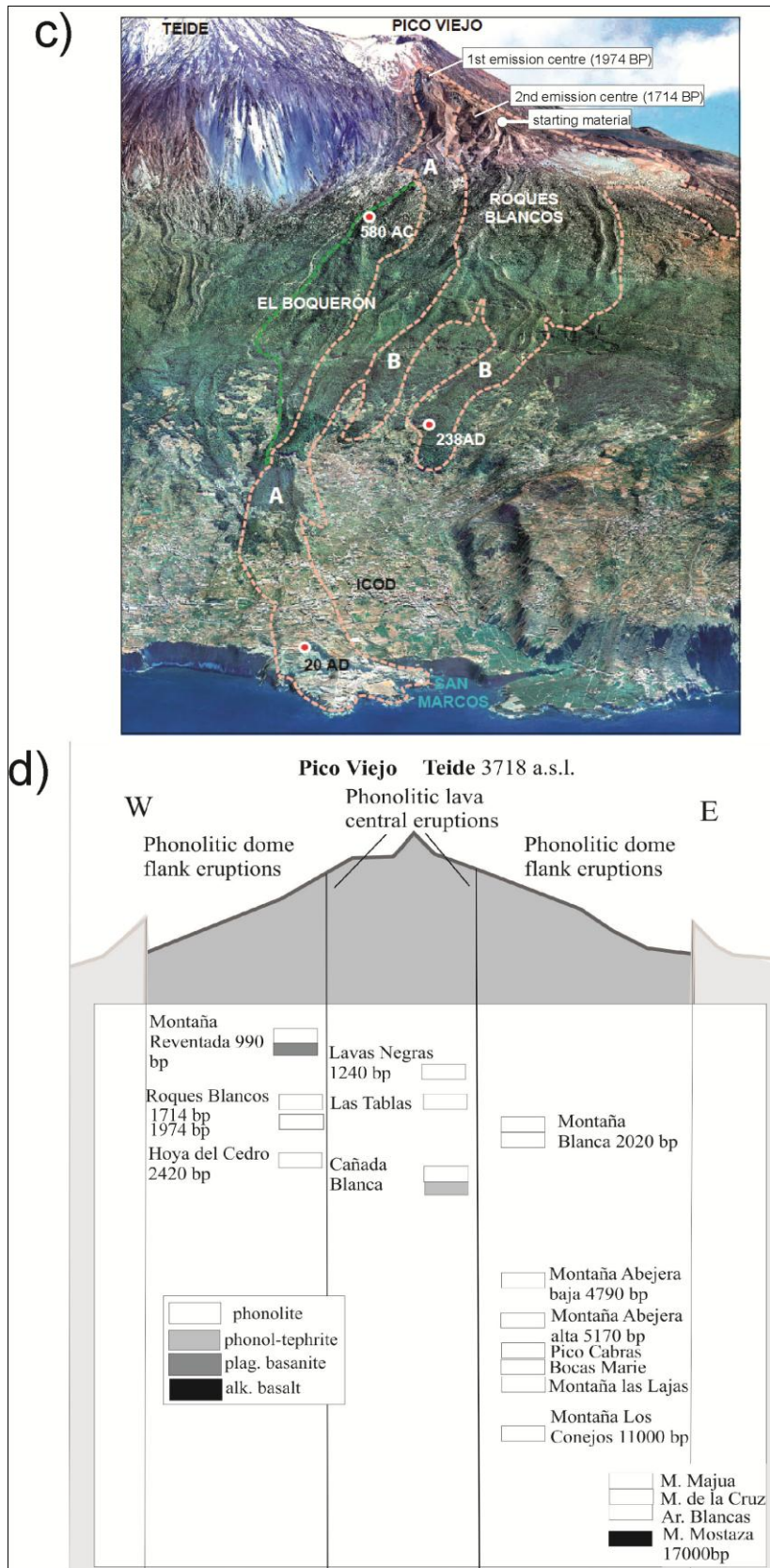


Figure 1. a) Geographic location of the Canary Islands and simplified geological map of Tenerife showing the products of the ancient basaltic shield, the las Cañadas Caldera depression and the actual volcanic complex of Teide (T), Pico Viejo (PV), the vent and

distribution of the Roques Blancos eruption products (Modified from Ablay and Martí, 2000).b) geological map of the flank dome eruptions of the Teide-Pico Viejo volcano and calibrated ages (modified from Carracedo et al., 2007);c) W view picture of the Roques Blancos flank dome and location of the corresponding vents (modified from Carracedo and Rodríguez-Badiola, 2006); d) Summary of the last 17.000 yr stratigraphy of the Teide-Pico Viejo volcanic complex (Modified from Ablay and Martí, 2000; Geochronology from Carracedo et al., 2007). Note the difference in the number of phonolitic events from Pico Teide central eruptions compared to those from flank vents.

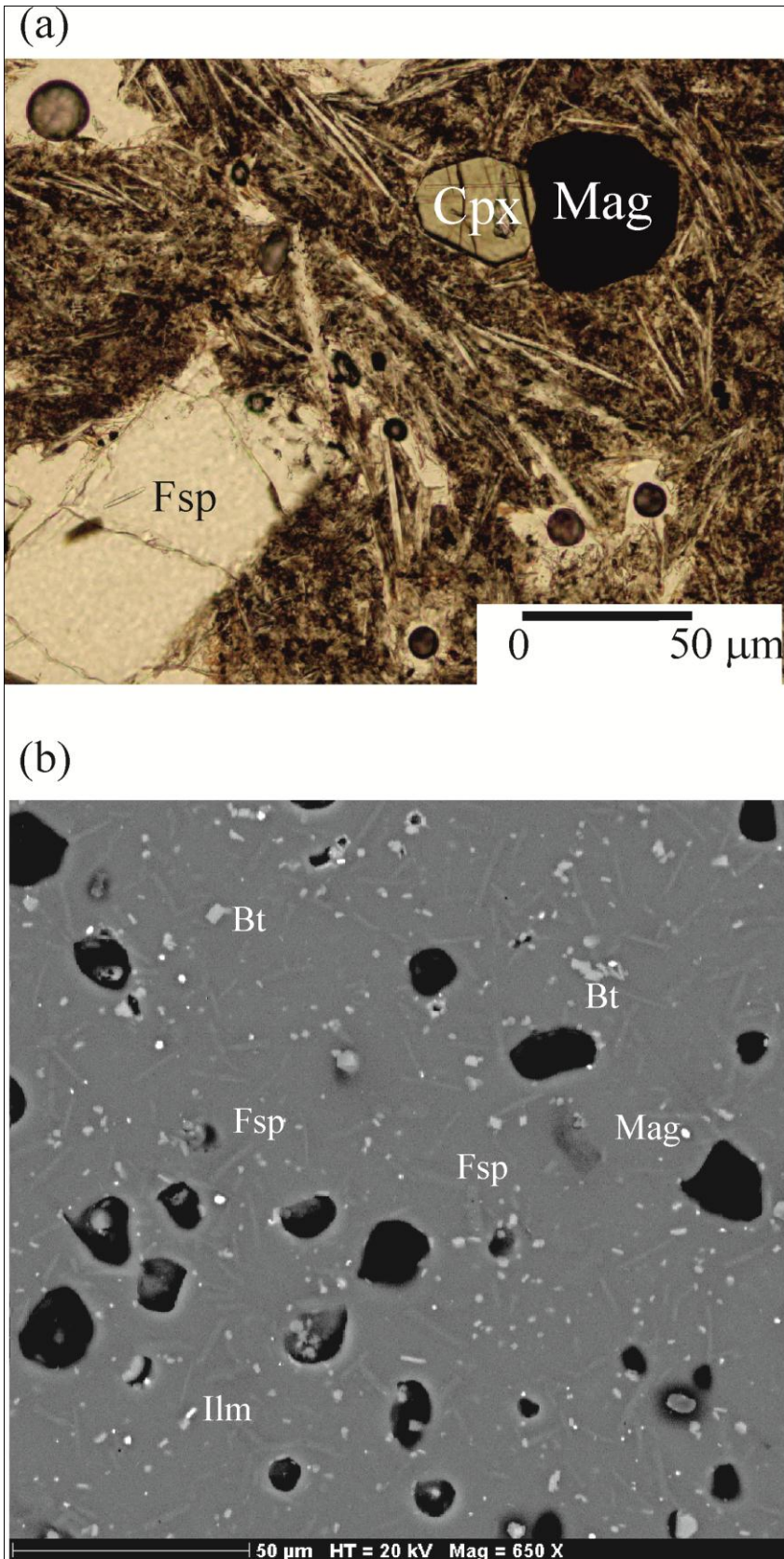


Figure 2. Photomicrograph of the Roques Blancos phonolite (Fsp: feldspar, Cpx: clinopyroxene, Mag: magnetite); b) Backscattered SEM image of an experimental

charge containing magnetite (mag), ilmenite (ilm), biotite (bt) and feldspar (fsp).
Crystals are euhedral, small and unzoned.

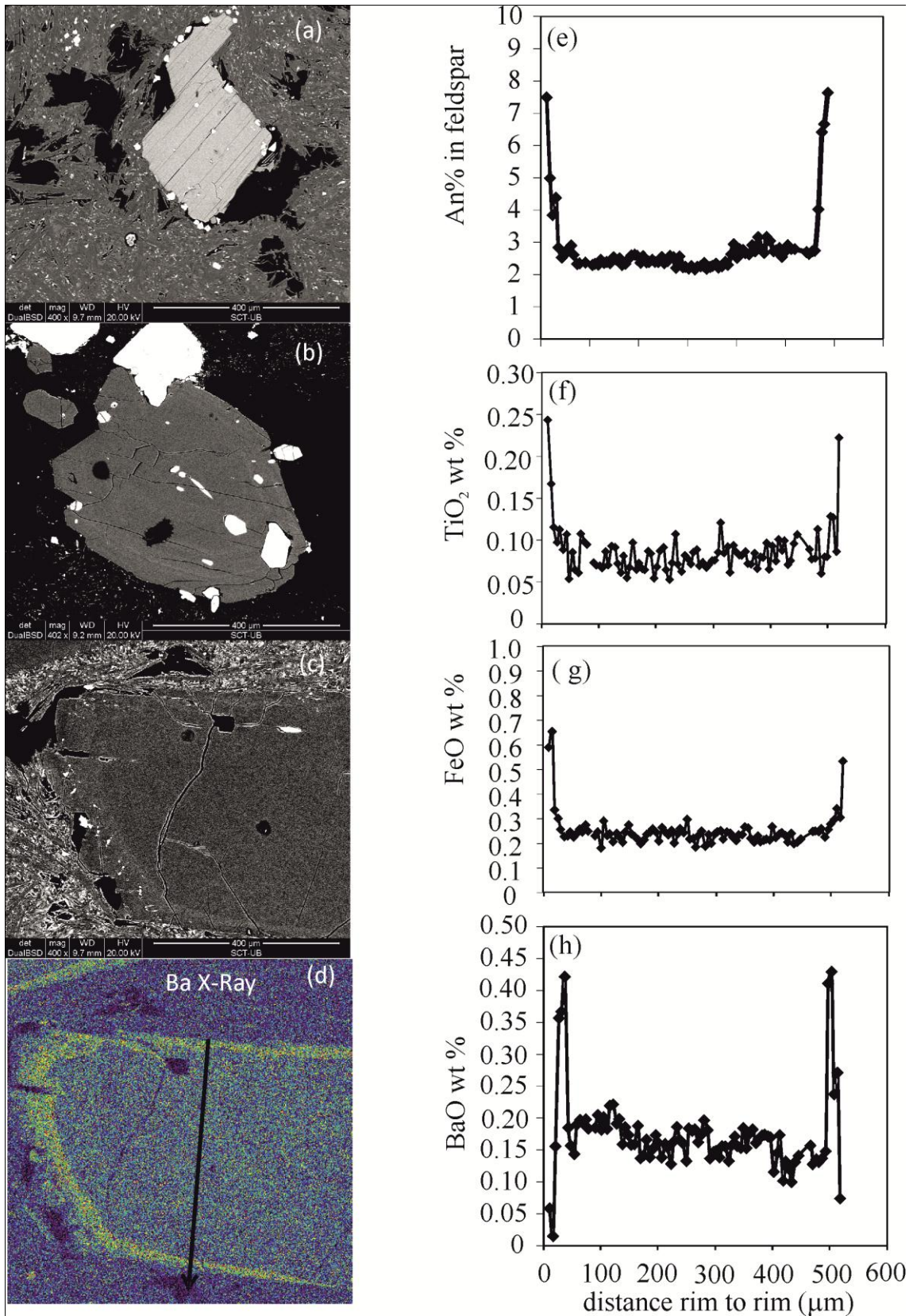


Figure 3. Example of Electron Microprobe compositional profile (rim to rim) of a natural feldspar showing a) variation in An content, b) TiO₂ wt%, c) FeO* wt% and

BaO wt% content. Note that the increase in An content towards the borders of the crystal is coupled with an increase in FeO, TiO₂ and BaO (see text for details).

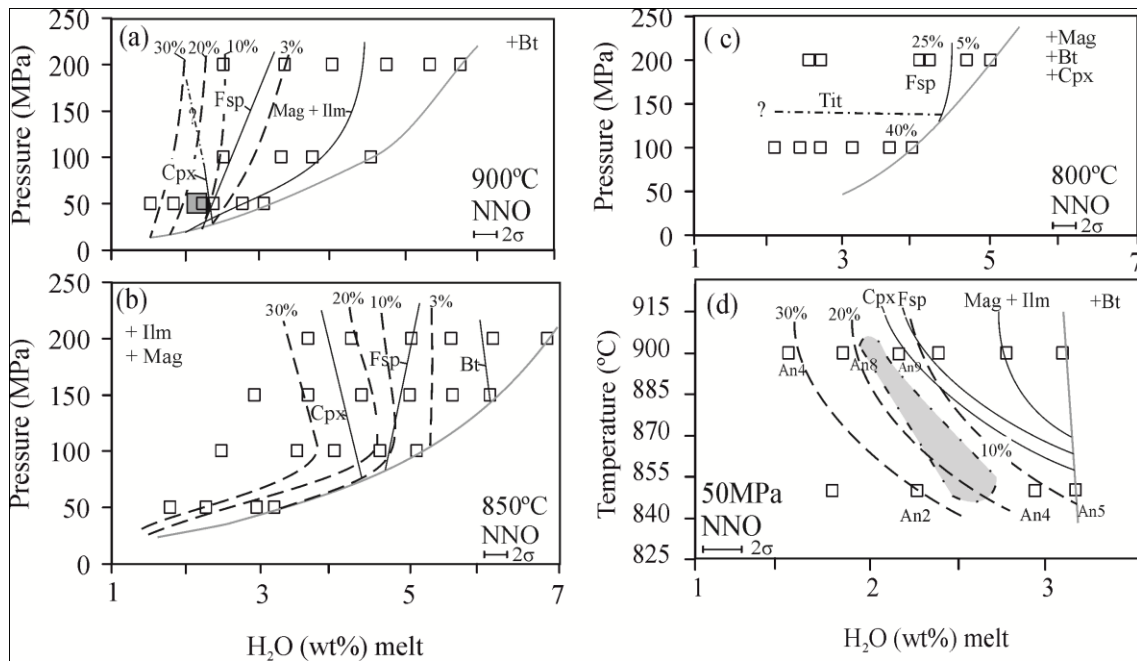


Figure 4. Isothermal phase relations of the Roques Blancos phonolite at a) 900°C and $f_{O_2} \sim NNO$; b) 850°C and $f_{O_2} \sim NNO$; c) 800°C and $f_{O_2} \sim NNO$ for different pressures and water contents in the melt; d) Isobaric phase relations (50 MPa and $f_{O_2} \sim NNO$) for various temperatures and water contents in the melt. Mag: magnetite, Bt: biotite, Cpx: clinopyroxene, ilm: ilmenite, tit: titanite, fsp: alkali feldspar. Dashed lines are estimated phase boundaries. Numbers above dashed lines indicate crystal content in wt (%). Label An below squares in plate d indicates the An content of experimental feldspars in the charge. Dashed and dotted lines in plates a and c indicate estimated phase boundaries for cpx and tit. Grey band in plate a and d shows the region where the phenocrysts content and mineral assemblage of the natural obsidian are reproduced (see text for details).

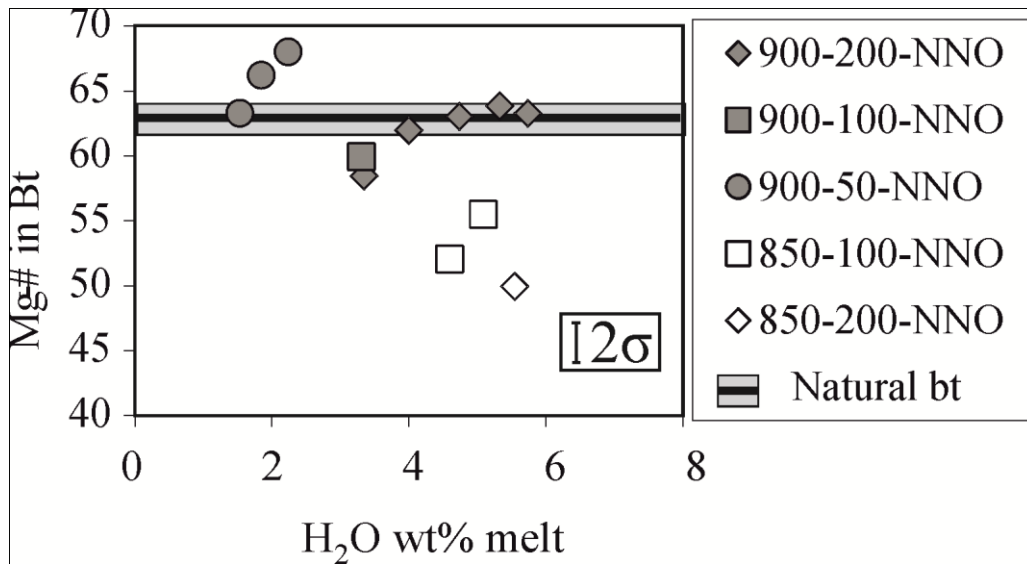


Figure 5. a) Variation of the Mg# with water content in the melt of natural and experimental biotites. Black line and grey horizontal bar shows the natural composition. Numbers next to symbols in the legend indicate temperature, pressure and fO_2 conditions.

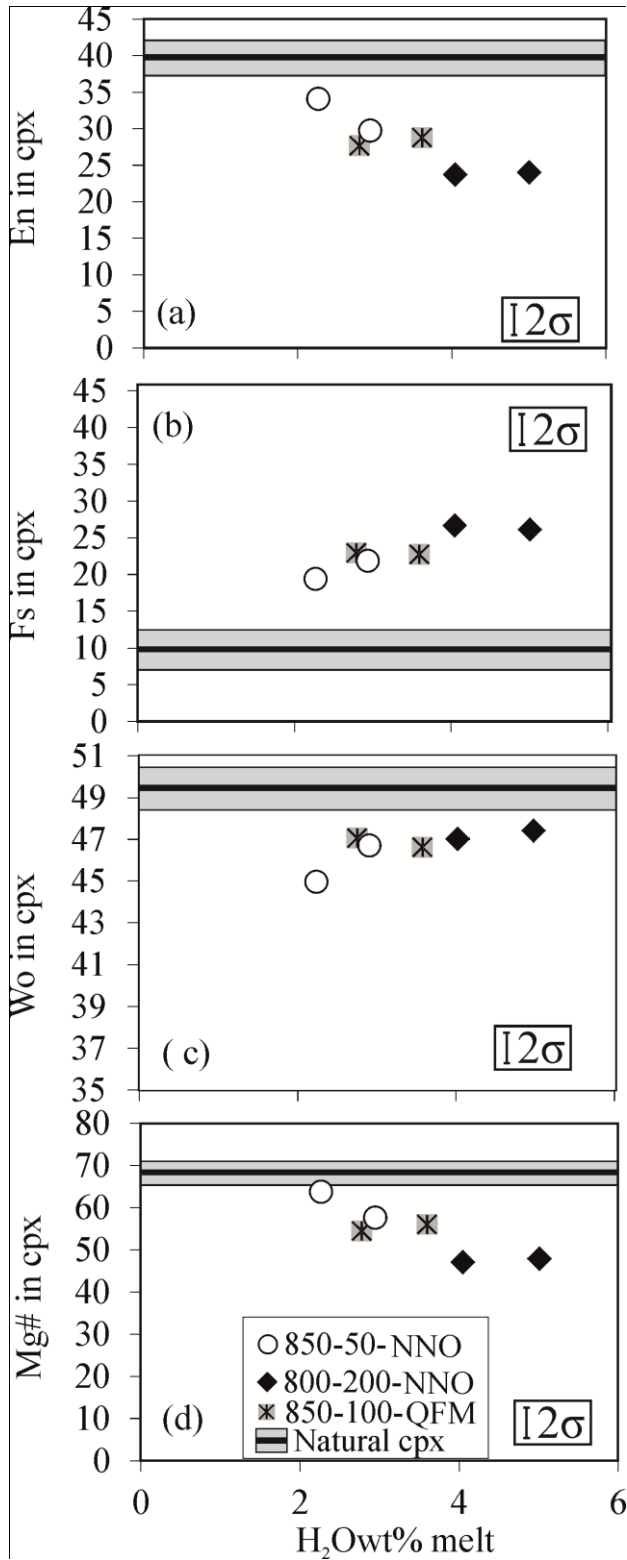


Figure 6. Variation of a) En content, b) Fs content, c) Wo content and d) Mg# of experimental and natural clinopyroxenes with water content in the melt. Black line and grey horizontal bar shows the natural composition. Numbers next to symbols in the legend indicate temperature, pressure and fO_2 conditions.

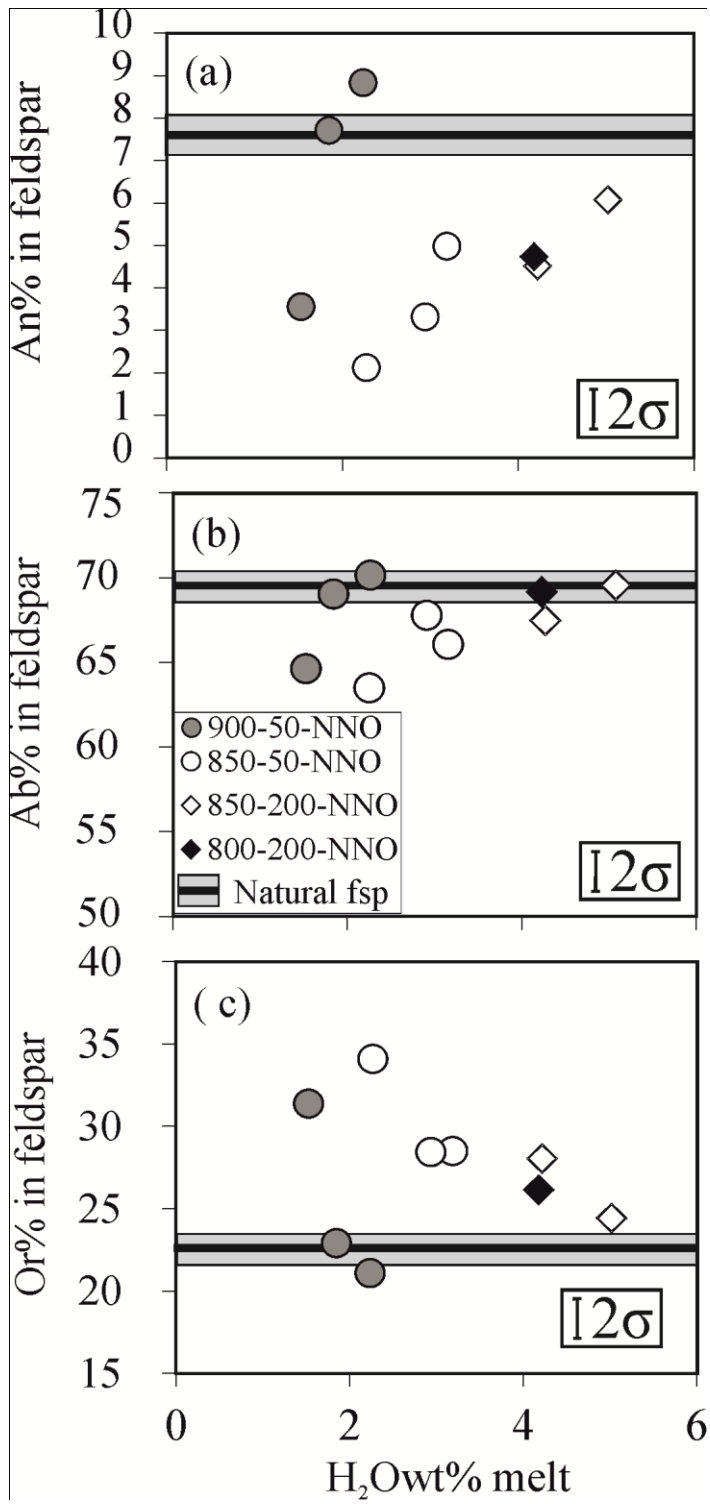


Figure 7. Variation of a) Anorthite content, b) albite content and c) orthoclase content in natural and experimental feldspars with water content in the melt. Black line and grey horizontal bar shows the natural composition. Numbers next to symbols in the legend indicate temperature, pressure and fO_2 conditions.

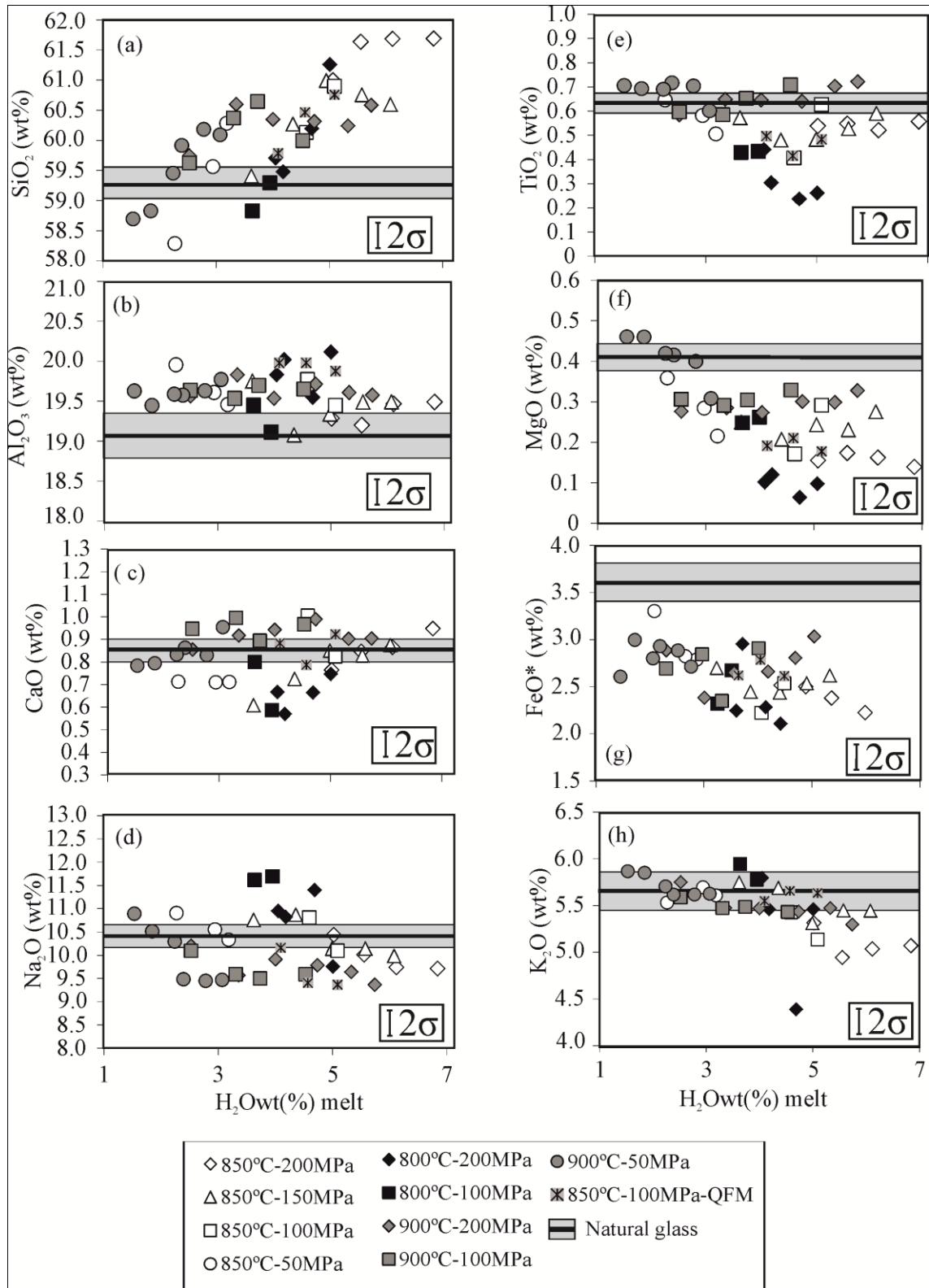


Figure 8. Glass compositional variations of major and minor oxides with water content in the melt (plates a to h). Black line and grey horizontal bar shows the natural composition. Numbers next to symbols in the legend indicate temperature, pressure and fO_2 conditions.

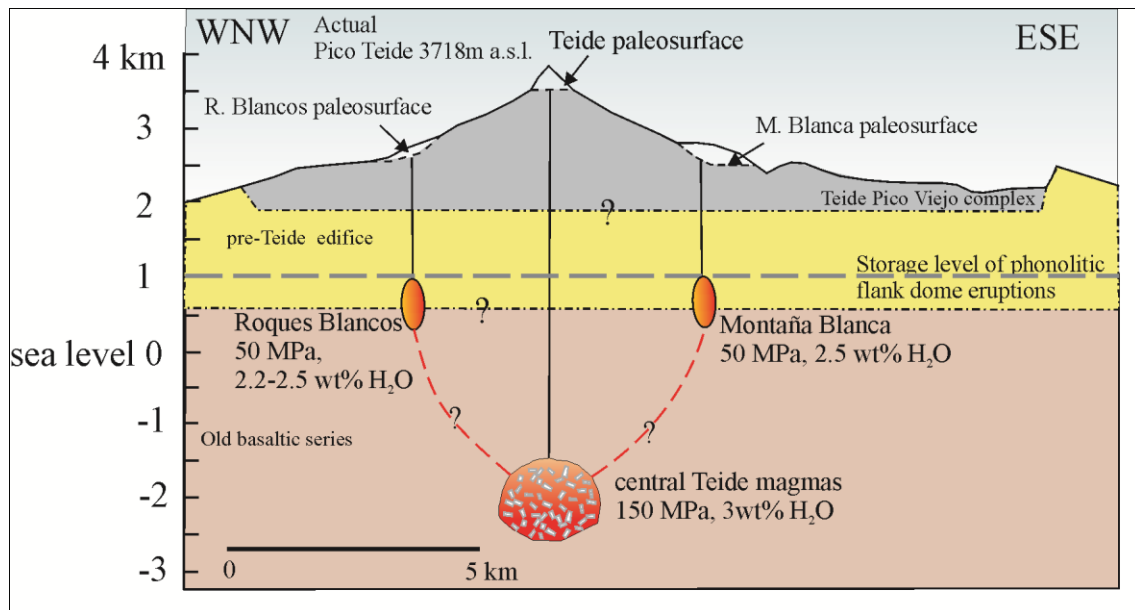


Figure 9. WNW-ESE cross section of the Teide-Pico Viejo stratovolcano showing the the location of the magmatic reservoirs for central Teide magmas (Andújar et al. 2010), Montaña Blanca (Andújar and Scaillet, 2012a) and Roques Blancos (this work). Magma reservoir volumes are not at scale (modified from Andújar and Scaillet, 2012a).

Table 1: Major element compositions (in wt%) of bulk-rock, glass, and minerals of the natural sample, and starting material.

	bulk rock a	starting material b	calculated glass c	sd	magnetite	sd	anorthoclase	sd	diopside	sd	biotite	sd	ilmenite	sd
n		15			6		17		8		10		6	
SiO ₂	59,38	59,64	59,23	0,33	0,08	0,01	65,11	0,40	51,36	0,41	36,66	0,28	0,05	0,01
TiO ₂	0,66	0,74	0,63	0,06	16,71	0,58	0,09	0,02	0,85	0,13	7,31	0,15	48,45	0,22
Al ₂ O ₃	18,89	19,41	19,01	0,23	1,00	0,01	19,72	0,29	1,37	0,18	12,55	0,15	0,10	0,00
MgO	0,41	0,48	0,41	0,05	2,09	0,09	0,00	0,00	12,59	0,39	13,87	0,17	2,96	0,12
CaO	0,88	0,80	0,86	0,09	0,16	0,20	0,93	0,20	21,66	0,24	0,00	0,00	0,10	0,04
MnO	0,19	0,14	0,21	0,02	2,50	0,01	0,00	-	0,83	0,03	0,00	0,00	3,26	0,03
FeO*	3,41	3,39	3,62	0,18	72,13	0,23	0,25	0,03	10,07	0,52	14,60	0,19	42,95	0,55
Na ₂ O	9,90	9,90	10,37	0,19	-	-	7,94	0,19	1,16	0,08	1,07	0,12	-	-
K ₂ O	5,48	5,49	5,65	0,12	-	-	4,81	0,42	0,00	0,00	8,45	0,08	-	-
P ₂ O ₅	0,07	-	-	-	-	-	-	-	-	-	-	-	-	-
Cl	0,30	-	-	-	-	-	-	-	-	-	-	-	-	-
F	0,12	-	-	-	-	-	-	-	-	-	-	-	-	-
Original Sum	99,69	100,0	100,0		94,7	0,2	98,9	0,3	99,9	0,6	94,5		97,9	0,0
Mg#			16,96		4,90				69,03	1,01	62,87	0,39		
An							4,44	0,95						
Ab							68,30	1,47						
Or							27,26	2,35						
Wo									49,6	0,3				
En									40,1	1,1				
Fs									10,3	1,2				
Phase proportions (wt%)			85,60		0,30		13,70		0,08		0,30		0,10	

Thermo-Oxybarometric results after Sauerzapf et al. (2008)

n. pairs	6	sd
T(°C)	895,37	4,8
ΔNNO ^d	-0,19	0,10
log fO ₂	-12,19	0,02

a: Bulk rock composition of the natural sample analysed by ICP-MS.

b: Electron Microprobe analysis of the starting glass added to the capsules.

c: Composition of the residual melt calculated by mass balance using the composition and abundance of the mineral phases and the bulk rock.

sd: Standard deviation.

n: Number of analysis.

*: Total iron reported as Fe²⁺.

Mg# = 100[Mg/(Mg+Fe*)].

Or, Ab, and An end- members calculated as in Deer et al. (1972)

End members for clinopyroxene (En, Fs, Wo) calculated as in Morimoto (1989).

phase proportions calculated as weight %.

d: Values for NNO buffer after Pownceby & O'Neill (1994)

Table 2: Experimental conditions and run products

NNO experiments

Run	XH ₂ Owt% _{in}	H ₂ Owt% _{melt}	<i>f</i> H ₂ (bar)	log <i>f</i> O ₂ (bar)	Δ NNO	aH ₂ O ^c	phase assemblage	Σr ₂
850°C,200MPa,162h		b	9.14 ^c	-12,69	0,20			
RB1	1,00	6,84		-12,71	0,14	0,98	(98.2)gl+(1.6)mag+(0.2)ilm	1,03
RB2	0,89	6,12		-12,90	-0,05	0,78	(98.2)gl+(1.4)mag+(0.4)ilm	0,90
RB3	0,81	5,55		-13,07	-0,22	0,65	(93.0)gl+(1.0)mag+(trace)ilm+(6.0)bt	1,20
RB4	0,73	5,02		-13,24	-0,39	0,53	(94.7)gl+(0.3)mag+(0.3)ilm+(4.7)bt+(trace)fsp	0,32
RB5	0,62	4,22		-13,55	-0,70	0,37	gl+mag+ilm+bt+fsp	n.d
RB6	0,53	3,63		-13,80	-0,95	0,28	gl+mag+ilm+bt+fsp+cpx	n.d
850°C,150MPa,233h		b	6,47 ^d	-12,76	0,13			
RB25	1,00	6,08		-12,76	0,10	1,00	(97.3)gl+(0.7)mag+(trace)ilm+(2.0)bt	0,06
RB26	0,92	5,57		-12,88	-0,02	0,87	(96.7)gl+(0.6)mag+(trace)ilm+(2.74)bt	0,06
RB27	0,82	4,99		-13,07	-0,21	0,70	(96.5)gl+(0.1)mag+(trace)ilm+(3.4)bt	0,22
RB28	0,72	4,36		-13,31	-0,45	0,53	(78.7)gl+(0.7)mag+(trace)ilm+(3.6)bt+(17.0)fsp	0,33
RB29	0,60	3,62		-13,63	-0,77	0,37	(75.5)gl+(1.2)mag+(trace)ilm+(1.6)bt+(20.9)fsp+(0.8)cpx	0,05
RB30	0,48	2,94		-13,99	-1,12	0,24	gl+mag+ilm+bt+fsp+cpx	n.d.
850°C,100MPa,195h		b	5,6 ^d	-12,88	0,01			
RB13	1,00	5,09		-12,87	0,00	1,00	(95.9)gl+(0.7)mag+(trace)ilm+(3.4)bt	0,21
RB14	0,90	4,60		-12,97	-0,10	0,89	(78.9)gl+(1.3)mag+(trace)ilm+(2.6)bt+(17.2)fsp	0,12
RB15	0,78	3,99		-13,22	-0,35	0,67	(72.7)gl+(1.5)mag+(trace)ilm+(3.1)bt+(22.7)fsp+(trace)cpx	0,12
RB16	0,69	3,49		-13,45	-0,58	0,51	gl+mag+ilm+bt+fsp+cpx	n.d.
RB18	0,49	2,48		-14,03	-1,16	0,26	gl+mag+ilm+bt+fsp+cpx	n.d.
850°C,50MPa,389h		b	2,42 ^c	-12,71	0,18			
RB31	1,00	3,19		-12,84	0,04	0,86	(92.3)gl+(0.5)mag+(0.1)ilm+(2.2)bt+(4.8)fsp+(0.1)cpx	0,06
RB32	0,92	2,94		-12,98	-0,10	0,73	(82.8)gl+(1.0)mag+(trace)ilm+(1.5)bt+(14.4)fsp+(0.3)cpx	0,01
RB34	0,71	2,27		-13,42	-0,54	0,44	(70.8)gl+(0.9)mag+(trace)ilm+(1.4)bt+(26.4)fsp+(0.5)cpx	0,10
RB35	0,56	1,79		-13,81	-0,93	0,28	gl+mag+ilm+bt+fsp+cpx	n.d.
800°C,205 MPa,114h		b	7,22 ^c	-13,71	0,19			
RB49	1,00	5,01		-13,70	0,16	0,93	(95.9)gl+(1.3)mag+(2.5)bt+(0.3)cpx	0,38
RB50	0,94	4,69		-13,81	0,06	0,85	(95.4)gl+(0.5)mag+(3.3)bt+(0.8)cpx	0,50
RB51	0,84	4,18		-13,97	-0,11	0,75	(76.9)gl+(0.6)mag+(2.4)bt+(1.0)cpx+(19.2)fsp	0,19
RB52	0,81	4,05		-14,10	-0,24	0,62	(73.5)gl+(1.5)mag+(1.6)bt+(0.5)cpx+(22.9)fsp	0,07
RB53	0,54	2,72					gl+mag+bt+cpx+fsp	n.d.
RB54	0,51	2,56					gl+mag+bt+cpx+fsp	n.d.
800°C,100MPa,145h		b	4,92 ^d	-13,87	0,03			
RB61	1,00	3,95		-13,87	0,03		(61.6)gl+(1.4)mag+(2.8)bt+(0.5)cpx+(33.7)fsp+(trace)tit	0,14
RB62	0,92	3,64		-13,93	-0,05		(60.7)gl+(1.9)mag+(1.7)bt+(trace)cpx+(35.7)fsp+(trace)tit	0,08
RB63	0,80	3,14					gl+mag+bt+cpx+fsp+tit	n.d
RB64	0,69	2,71					gl+mag+bt+cpx+fsp+tit	n.d.
RB65	0,62	2,44					gl+mag+bt+cpx+fsp+tit	n.d.
RB66	0,53	2,09					gl+mag+bt+cpx+fsp+tit	n.d.

900°C,200MPa,164h		a	8,36 ^c	-11,69	0,27			
RB85	1,00	5,74		-12,11	-0,19	0,69	(97.5)gl+(2.5)bt	0,73
RB86	0,93	5,33		-12,23	-0,31	0,60	(97.5)gl+(2.5)bt	0,43
RB87	0,83	4,74		-12,44	-0,52	0,47	(97.3)gl+(2.7)bt	0,39
RB88	0,70	4,00		-12,74	-0,81	0,34	(97.8)gl+(0.9)mag+(trace)ilm+(1.3)bt	0,06
RB89	0,58	3,35		-13,04	-1,12	0,24	(97.7)gl+(1.4)mag+(trace)ilm+(0.4)bt	0,35
RB90	0,44	2,53		-13,52	-1,60	0,14	(88.1)gl+(0.9)mag+(trace)ilm+(0.7)bt+(10.3)fsp	0,07
900°C,100MPa,188h		a	4,89 ^d	-11,81	0,15			
RB 91	1,00	4,53		-11,94	0,00	0,86	(98.4)gl+(1.6)bt	0,34
RB 93	0,82	3,73		-12,27	-0,33	0,59	(98.2)gl+(1.5)mag+(trace)ilm+(0.3)bt	0,37
RB 94	0,73	3,31		-12,48	-0,54	0,46	(98.2)gl+(0.6)mag+(0.2)ilm+(0.7)bt	0,30
RB 95	0,56	2,53		-12,94	-1,00	0,27	(89.8)gl+(1.0)mag+(trace)ilm+(0.3)bt+(8.9)fsp	0,11
900°C,50MPa,284h		a	3,53 ^c	-11,75	0,21			
RB 96	1,00	3,07		-11,95	0,01	0,80	(98.2)gl+(1.8)bt	0,30
RB 97	0,91	2,78		-12,11	-0,16	0,66	(98.4)gl+(1.6)bt	0,57
RB 98	0,78	2,39		-12,37	-0,41	0,49	(98.5)gl+(0.7)mag+(trace)ilm+(0.8)bt	0,26
RB 99	0,73	2,24		-12,48	-0,52	0,43	(85.0)gl+(1.3)mag+(0.1)ilm+(0.1)bt+(trace)cpx+(13.5)fsp	0,08
RB 100	0,60	1,85		-12,79	-0,84	0,30	(74.3)gl+(1.3)mag+(trace)ilm+(0.4)bt+(0.2)cpx+(23.8)fsp	0,10
RB 101	0,50	1,53		-13,09	-1,13	0,21	(67.8)gl+(1.8)mag+(trace)ilm+(0.6)bt+(0.2)cpx+(29.6)fsp	0,09
QFM experiments								
850°C,100MPa,188h		b	6,66 ^c	-13,03	-0,14			
RB 73	1,00	5,09		-13,25	-0,38	1,00	(98.0)gl+(0.7)mag+(0.5)ilm+(0.8)bt	0,70
RB 74	0,90	4,57		-13,32	-0,45	0,89	(98.3)gl+(0.4)mag+(0.7)ilm+(trace)bt+(0.6)cpx	0,58
RB 75	0,80	4,09		-13,48	-0,61	0,67	(88.7)gl+(0.9)mag+(trace)ilm+(0.9)bt+(0.5)cpx+(9.0)fsp	0,25
RB 76	0,71	3,61		-13,73	-0,86	0,51	gl+mag+ilm+bt+cpx+fsp	n.d.
RB 77	0,55	2,80		-13,88	-1,01	0,31	gl+mag+ilm+bt+cpx+fsp	n.d.
RB 78	0,53	2,70		-14,15	-1,28	0,26	gl+mag+ilm+bt+cpx+fsp	n.d.

XH₂Owt%in:initial H₂O/(H₂O+CO₂) in the charge

H₂Owt%melt: water content in the melt a: determined by FTIR, b:determined by the solubility model of Papale et al. (2006)

fH₂(bar):hydrogen fugacity of the experiment. c:determined by using NiPd alloy sensors, d:calculated using the data obtained from succesfull NiPd alloys (see text for details)

log fO₂(bar): logarithm of the oxygen fugacity calculated from the experimental fH₂

Δ NNO:log fO₂-log fO₂ of the NNO buffer calculated at P and T (Pownceby & O'Neill,1994)

e:aH₂Ocalculated by using H₂Owt% at saturation/ H₂Owt% in the melt (see text for details)

n.d.: not determined

phase assemblage: numbers in brackets indicate the phase abundance in the charge in weight %

Gl:glass, Mag:magnetite,Bt:biotite,Cpx:clinopyroxene, Ilm:ilmenite,Fsp:alkali feldspar, Tit:titanite

Table 3: FTIR data of experimental runs

Sample	n	Thickness(μm)	sd	5200(cm^{-1})	sd	4500(cm^{-1})	sd	Density(g/l)a	sd	H ₂ O($\text{wt}\%$)b	sd
RB85	3	197,0	2,1	0,05	0,00	0,01	0,00	2579,5	12,0	5,72	0,60
RB91	3	135,0	3,5	0,07	0,00	0,03	0,00	2641,5	2,6	4,53	0,12
RB96	3	91,5	2,6	0,03	0,00	0,02	0,00	2672,0	5,3	3,07	0,23

n: number of spectra

sd: standard deviation

5200(cm^{-1}): Absorbance intensity from the 5200 peak

4500(cm^{-1}): Absorbance intensity from the 4500 peak

a: density of the melt calculated as in

b: Total H₂O($\text{wt}\%$) dissolved in the melt calculated as the sum of the water from 5200 and 4500 peaks

Table 4: Composition (wt%) and end-members of experimental mineral phases

Magnetite

	SiO ₂	TiO ₂	Al ₂ O ₃	MgO	CaO	MnO	FeO	Na ₂ O	K ₂ O	Sum	Mg#	wt%gl
RB32(3)	-	17,44	0,91	1,54	0,00	3,02	77,13	-	-	100,0	3,43	1,20
sd	-	0,29	0,01	0,09	0,00	0,10	0,26	-	-	0,0	-	
RB16	-	13,75	2,10	1,75	0,00	3,53	78,87	-	-	100,0	3,81	2,10

Ilmenite

	SiO ₂	TiO ₂	Al ₂ O ₃	MgO	CaO	MnO	FeO	Na ₂ O	K ₂ O	Sum	Mg#	wt%gl
RB13(3)	-	49,49	0,10	2,22	0,00	3,75	44,47	-	-	100,0	-	0,50
sd	-	0,15	0,05	0,15	0,00	0,10	0,13	-	-	0,0	-	
RB14(4)	-	50,10	0,12	2,31	0,00	4,19	43,28	-	-	100,0	-	2,30
sd	-	0,42	0,06	0,06	0,00	0,08	0,48	-	-	0,0	-	
RB15	-	50,47	0,07	2,43	0,00	4,86	42,22	-	-	100,0	-	3,00
RB3	-	48,72	0,07	1,98	0,00	3,47	45,72	-	-	100,0	-	1,10
RB77(2)	0,0	0,00	51,06	0,00	1,78	4,56	42,85	-	-	100,0	-	

Biotite

	SiO ₂	TiO ₂	Al ₂ O ₃	MgO	CaO	MnO	FeO	Na ₂ O	K ₂ O	Sum	Mg#	wt%gl
RB3	37,7	5,76	13,93	18,67	0,54	10,45	0,07	1,61	8,05	96,7	49,93	-
sd	0,6	0,36	0,26	0,28	0,05	0,66	0,05	0,53	0,30	0,7	1,22	-
RB13(5)	37,3	5,76	13,63	16,71	0,56	11,69	0,05	1,19	8,14	95,0	55,48	-
sd	0,9	0,38	0,21	0,48	0,04	0,67	0,03	0,31	0,28	0,4	1,30	-
RB14(3)	38,9	5,84	13,62	16,98	0,56	10,33	0,09	1,94	8,02	96,3	52,03	-
sd	0,5	0,36	0,24	0,86	0,06	0,60	0,07	0,44	0,31	1,3	0,20	-
RB85	35,9	4,74	14,54	15,23	0,54	14,70	0,00	1,02	8,86	96,5	63,25	-
RB86	40,8	4,74	15,76	13,03	0,57	12,89	0,11	1,61	8,07	97,6	63,82	-
RB87	35,8	5,73	15,56	14,72	0,24	14,07	0,00	1,02	8,94	97,1	63,02	-
RB88(2)	40,5	5,75	14,89	12,68	0,43	11,58	0,13	1,98	8,18	97,1	61,95	-
sd	0,7	0,24	0,45	0,76	0,08	0,72	0,02	0,34	0,36	0,5	0,05	-

RB89(2)	36,6	5,58	16,68	14,17	0,36	11,17	0,07	1,41	8,07	95,1	58,43	-
sd	0,5	0,11	0,67	0,57	0,06	0,25	0,08	0,05	0,02	0,8	0,43	-
RB94	38,2	6,18	14,59	14,51	0,47	12,16	0,03	1,34	8,16	96,6	59,90	-
RB99(2)	36,2	5,54	15,54	12,34	0,41	14,70	0,04	1,22	8,28	95,2	67,98	-
sd	0,5	0,41	0,22	0,44	0,13	0,22	0,01	0,14	0,21	0,6	0,45	-
RB100 (2)	37,5	6,39	14,71	12,45	0,38	13,66	0,02	1,22	8,53	96,4	66,17	-
sd	0,3	0,14	0,90	0,22	0,14	0,11	0,02	0,20	0,13	0,5	0,58	-
RB101	39,0	5,71	15,01	13,31	0,52	12,85	0,08	2,13	8,40	97,0	63,25	-

Clinopyroxene

	SiO ₂	TiO ₂	Al ₂ O ₃	MgO	CaO	MnO	FeO	Na ₂ O	K ₂ O	Sum	Mg#	wt%gl	En	Fs	Wo
RB32(4)	48,4	2,45	3,15	9,36	20,49	1,00	12,27	1,62	0,09	98,8	57,62	-	29,7	21,8	46,7
sd	0,3	0,22	0,21	0,20	0,14	0,06	0,14	0,13	0,02	0,3	0,59	-	0,5	0,2	0,3
RB34(4)	49,9	1,60	1,85	11,43	21,00	0,97	11,58	1,66	0,00	100,0	63,75	-	34,0	19,4	44,9
sd	0,3	0,30	0,83	0,32	0,80	0,11	0,21	0,32	0,00	0,0	0,36	-	0,3	0,4	0,9
RB49(3)	50,3	0,79	1,30	7,95	21,87	1,48	15,42	0,93	0,00	100,0	47,89	2,80	24,0	26,1	47,4
sd	0,6	0,30	0,32	0,36	0,07	0,12	0,45	0,07	0,00	0,0	1,85	1,73	1,0	0,9	0,3
RB52	50,4	0,67	1,18	7,59	20,96	1,49	15,23	1,38	0,14	99,0	47,04	-	23,7	26,7	47,0
RB76(2)	51,0	1,58	4,04	8,65	19,60	1,17	12,17	1,91	0,47	100,5	55,89	-	28,6	22,6	46,6
sd	0,4	0,48	0,88	0,11	0,47	0,05	0,45	0,18	0,08	1,3	1,24	-	0,8	0,5	0,4
RB77(2)	50,1	0,96	1,93	8,75	20,64	1,29	12,92	1,41	0,19	98,2	54,68	-	27,7	23,0	47,0
sd	0,4	0,12	0,60	0,40	0,30	0,05	0,25	0,25	0,02	0,1	1,61	-	0,8	0,8	0,1

Feldspars

	SiO ₂	TiO ₂	Al ₂ O ₃	MgO	CaO	MnO	FeO	Na ₂ O	K ₂ O	Sum	Mg#	wt%gl	An	Ab	Or
RB4(2)	64,1	0,36	19,64	0,18	1,23	0,00	1,50	7,75	4,14	98,9	-	-	6,1	69,5	24,4
sd	0,7	0,14	0,48	0,02	0,04	0,00	0,54	0,20	0,09	0,8	-	-	0,0	0,0	0,1
RB5	64,4	0,44	19,24	0,17	0,94	0,00	1,04	7,76	4,90	98,9	-	-	4,5	67,5	28,0
RB31	65,9	0,20	19,64	0,03	1,08	0,02	0,53	7,72	5,03	100,1	-	-	5,12	66,41	28,5
RB32	67,1	0,18	20,02	0,00	0,71	0,03	0,41	7,80	4,94	101,2	-	-	3,45	68,13	28,4
RB34	63,5	0,33	19,64	0,16	0,46	0,25	1,60	7,64	6,19	99,8	-	-	2,12	63,82	34,1

RB51(3)	64,6	0,16	20,24	0,03	0,95	0,00	0,44	7,63	4,38	98,4	-	-	4,7	69,1	26,1
sd	0,1	0,01	0,36	0,02	0,01	0,00	0,22	0,06	0,07	0,5	-	-	0,0	0,4	0,5
RB99	64,6	0,16	20,89	0,03	1,92	0,00	0,12	8,40	3,83	100,1	-	-	8,8	70,1	21,1
RB100	64,3	0,23	20,78	0,00	1,66	0,13	0,52	8,26	4,14	100,1	-	-	7,7	69,4	22,9
RB101(2)	64,1	0,28	19,60	0,07	0,78	0,19	0,73	7,54	5,53	99,3	-	-	3,69	64,95	31,4
	0,7	0,02	0,12	0,00	0,04	0,04	0,16	0,22	0,06	0,6	-	-	0,12	0,29	0,41

numbers in brackets indicate the number of analysis.

sd: Standard deviation

* Total Iron reported as FeO

$Mg\# = 100[Mg/(Mg+Fe^*)]$

wt% glass: Clinopyroxene compositions are re-calculated due to glass contamination (see text for details)

and here we indicate the wt% glass subtracted to the original electron microprobe analysis

En, Fs, Wo: calculated as in Morimoto (1989)

$An = 100[Ca/(Ca+Na+K)]$; $Ab = 100[Na/(Ca+Na+K)]$; $Or = [100K/(Ca+Na+K)]$. End members calculated as in Deer et al. (1972).

Table 5: Experimental melt composition (wt%) normalized to 100% anhydrous basis

Run

NNO experiments

850°C,200MPa,162h

	SiO ₂	TiO ₂	Al ₂ O ₃	MgO	CaO	MnO	FeO*	Na ₂ O	K ₂ O	Sum	Mg#	original sum	Na ₂ O+K ₂ O	per-alk
RB1(4)	61,7	0,56	19,5	0,15	0,95	0,16	2,23	9,7	5,1	100	10,6	96,6	14,8	1,1
sd	0,9	0,04	0,4	0,04	0,02	0,04	0,24	0,3	0,1	-		0,5		
RB2(5)	61,7	0,52	19,5	0,16	0,87	0,15	2,38	9,7	5,0	100	10,8	96,7	14,8	1,1
sd	0,6	0,04	0,4	0,04	0,02	0,03	0,06	0,2	0,1	-		0,7		
RB3(4)	61,6	0,55	19,2	0,17	0,85	0,14	2,50	10,0	4,9	100	11,0	98,1	15,0	1,1
sd	0,5	0,14	0,0	0,05	0,08	0,03	0,29	0,1	0,19	-		0,4		
RB4(4)	60,9	0,54	19,3	0,16	0,76	0,18	2,51	10,4	5,3	100	9,9	98,9	15,8	1,2
sd	0,3	0,07	0,3	0,00	0,11	0,04	0,04	0,2	0,1	-		0,6		

850°C,150MPa,233h

RB25(9)	60,6	0,59	19,5	0,28	0,87	0,13	2,62	10,0	5,4	100	15,8	94,5	15,4	1,1
sd	0,3	0,12	0,2	0,03	0,05	0,06	0,14	0,3	0,2	-		0,7		
RB26(5)	60,8	0,53	19,5	0,23	0,83	0,04	2,54	10,1	5,4	100	14,0	96,1	15,6	1,2
sd	0,2	0,08	0,1	0,03	0,03	0,08	0,12	0,2	0,0	-		0,7		
RB27(4)	61,0	0,48	19,3	0,24	0,85	0,20	2,44	10,1	5,3	100	15,1	93,7	15,4	1,2
sd	0,3	0,04	0,3	0,04	0,10	0,08	0,16	0,2	0,0	-		0,6		
RB28(3)	60,3	0,48	19,1	0,21	0,72	0,23	2,45	10,9	5,7	100	13,1	95,6	16,6	1,3
sd	0,3	0,06	0,2	0,06	0,06	0,07	0,29	0,1	0,2	-		0,9		
RB29(6)	59,4	0,57	19,8	0,25	0,61	0,20	2,70	10,8	5,7	100	14,2	96,3	16,5	1,2
sd	0,3	0,09	0,1	0,02	0,08	0,07	0,27	0,2	0,1	-		0,6		

850°C,100MPa,195h

RB13(5)	60,9	0,63	19,4	0,29	0,82	0,15	2,53	10,1	5,1	100	17,0	95,5	15,2	1,1
sd	0,6	0,21	0,3	0,13	0,04	0,04	0,26	0,4	0,0	-		0,7		

RB14(1)	60,1	0,41	19,8	0,17	1,00	0,06	2,22	10,8	5,4	100	12,1	93,6	16,2	1,2
RB15(1)	60,8	0,41	20,0	0,17	1,01	0,06	2,25	9,9	5,5	100	12,1	96,2	15,3	1,1
850°C,50MPa,389h														
RB31(4)	60,3	0,51	19,5	0,22	0,71	0,11	2,79	10,3	5,6	100	12,1	95,6	15,9	1,2
sd	0,3	0,05	0,2	0,01	0,05	0,08	0,19	0,3	0,1	-		0,5		
RB32(3)	59,6	0,58	19,6	0,28	0,71	0,19	2,82	10,5	5,7	100	15,2	96,3	16,2	1,2
sd	0,2	0,05	0,2	0,04	0,10	0,09	0,17	0,1	0,1	-		0,4		
RB34(1)	58,3	0,65	20,0	0,36	0,71	0,31	3,30	10,9	5,5	100	16,2	97,2	16,4	1,2
800°C,205 MPa,114h														
RB49(4)	61,3	0,26	20,1	0,10	0,75	0,10	2,11	9,8	5,5	100	7,6	89,0	15,2	1,1
sd	0,5	0,02	0,2	0,03	0,06	0,01	0,03	0,2	0,3	-		0,6		
RB50(3)	60,2	0,24	19,5	0,06	0,66	0,12	2,28	11,4	4,4	100	4,8	90,7	15,8	1,2
sd	0,2	0,04	0,1	0,03	0,05	0,08	0,14	0,1	0,1	-		0,1		
RB51(3)	59,5	0,30	20,0	0,12	0,57	0,18	2,95	10,8	5,5	100	6,7	95,1	16,3	1,2
sd	0,5	0,06	0,2	0,02	0,05	0,04	0,23	0,1	0,3	-		0,7		
RB52(3)	59,7	0,44	19,8	0,10	0,67	0,08	2,25	11,0	5,8	100	7,5	95,5	16,7	1,2
sd	0,3	0,08	0,3	0,04	0,04	0,05	0,49	0,6	0,3	-		0,8		
800°C,100MPa,145h														
RB61(1)	59,3	0,43	19,1	0,26	0,59	0,18	2,67	11,7	5,8	100	14,8	96,6	17,5	1,3
RB62(1)	58,8	0,43	19,4	0,25	0,80	0,15	2,32	11,6	5,9	100	16,0	96,6	17,6	1,3
900°C,200MPa,164h														
RB85(4)	60,6	0,72	19,6	0,33	0,90	0,19	3,03	9,4	5,3	100	16,2	93,6	14,7	1,1

sd	1,0	0,08	0,1	0,02	0,09	0,18	0,36	0,6	0,1	-		0,4		
RB86(4)	60,2	0,70	19,6	0,30	0,90	0,33	2,81	9,6	5,5	100	15,9	94,0	15,1	1,1
sd	0,3	0,13	0,3	0,03	0,02	0,09	0,33	0,2	0,2	-		0,7		
RB87(5)	60,3	0,64	19,7	0,30	0,99	0,16	2,66	9,8	5,4	100	16,8	95,0	15,2	1,1
sd	0,1	0,07	0,2	0,05	0,02	0,16	0,16	0,0	0,1	-		0,7		
RB88(3)	60,3	0,65	19,5	0,27	0,94	0,23	2,65	9,9	5,5	100	15,5	94,6	15,4	1,1
sd	0,5	0,01	0,2	0,01	0,04	0,10	0,12	0,3	0,1	-				
RB89(3)	60,6	0,65	19,8	0,28	0,92	0,30	2,38	9,6	5,5	100	17,6	95,6	15,0	1,1
sd	0,2	0,08	0,0	0,00	0,06	0,06	0,43	0,2	0,0	-		0,5		
RB90(4)	59,7	0,58	19,6	0,28	0,85	0,16	2,89	10,2	5,8	100	14,6	96,7	15,9	1,2
sd	0,4	0,07	0,3	0,01	0,05	0,11	0,22	0,4	0,2	-		0,6		
900°C,100MPa,188h														
RB 91(4)	60,0	0,71	19,7	0,33	0,97	0,16	2,91	9,6	5,4	100	16,8	95,4	15,0	1,1
sd	0,4	0,05	0,3	0,04	0,10	0,07	0,20	0,4	0,2	-		0,6		
RB 93(3)	60,6	0,65	19,7	0,30	0,89	0,20	2,35	9,5	5,5	100	18,8	96,3	15,0	1,1
sd	0,1	0,09	0,1	0,04	0,09	0,16	0,31	0,3	0,1	-		0,7		
RB 94(6)	60,4	0,58	19,5	0,29	0,99	0,17	2,84	9,6	5,5	100	15,4	96,3	15,1	1,1
sd	0,1	0,12	0,2	0,03	0,05	0,18	0,13	0,1	0,2	-		0,4		
RB 95(3)	59,7	0,60	19,6	0,31	0,95	0,20	2,69	10,1	5,6	100	16,8	97,7	15,7	1,2
sd	0,4	0,02	0,3	0,03	0,10	0,18	0,40	0,4	0,2	-		0,1		
900°C,50MPa,284h														
RB 96(4)	60,1	0,60	19,8	0,31	0,95	0,20	2,71	9,5	5,6	100	16,8	97,0	15,1	1,1
sd	0,4	0,05	0,2	0,02	0,07	0,12	0,45	0,4	0,2	-		0,8		
RB 97(5)	60,2	0,70	19,6	0,40	0,83	0,17	2,88	9,4	5,6	100	19,8	97,7	15,1	1,1
sd	0,5	0,09	0,1	0,02	0,06	0,07	0,38	0,3	0,1	-		0,6		
RB 98(5)	59,9	0,72	19,6	0,42	0,86	0,18	2,93	9,5	5,6	100	20,2	97,9	15,1	1,1
sd	0,3	0,09	0,1	0,07	0,03	0,06	0,27	0,2	0,1	-		0,5		
RB 99(5)	59,5	0,69	19,6	0,42	0,83	0,11	2,80	10,3	5,7	100	21,1	97,6	16,0	1,2
sd	0,3	0,13	0,1	0,03	0,03	0,09	0,22	0,2	0,1	-		0,4		

RB 100(5)	58,8	0,69	19,4	0,46	0,79	0,18	3,00	10,5	5,8	100	21,5	97,8	16,4	1,2
sd	0,4	0,05	0,2	0,06	0,05	0,09	0,30	0,2	0,1	-		1,3		
RB 101(5)	58,7	0,70	19,6	0,46	0,78	0,17	2,60	10,9	5,9	100	24,0	98,4	16,8	1,2
sd	0,4	0,06	0,2	0,05	0,04	0,07	0,11	0,3	0,2	-		0,7		
QFM experiments														
850°C,100MPa,188h														
RB 73(3)	60,8	0,48	19,9	0,18	0,92	0,17	2,61	9,4	5,6	100	10,8	93,7	15,0	1,1
sd	0,3	0,03	0,0	0,03	0,06	0,15	0,09	0,1	0,2	-		0,9		
RB 74(3)	60,5	0,41	20,0	0,21	0,79	0,24	2,78	9,4	5,7	100	11,9	93,9	15,1	1,1
sd	0,3	0,03	0,0	0,03	0,06	0,15	0,09	0,1	0,2	-		0,8		
RB 75(3)	59,8	0,50	20,0	0,19	0,88	0,23	2,62	10,2	5,6	100	11,5	95,0	15,7	1,1
sd	0,3	0,03	0,0	0,03	0,06	0,15	0,09	0,1	0,2	-		0,9		

numbers in brackets indicate the number of analysis

All analyses are normalized to 100% anhydrous. Original totals are reported (original sum)

sd: standard deviation

Mg#: magnesium number of the melt calculated as $Mg\# = 100 * (Mg / (Mg + Fe))$ in moles

per-alk: per-alkalinity calculated as $(Na + K) / Al$ in moles

FeO*: Total iron reported as Fe^{2+}